CrossMark

JWST MIRI/Medium Resolution Spectrograph (MRS) Observations and Spectral Models of the Underluminous Type Ia Supernova 2022xkq

J. M. DerKacy[1], C. Ashall[1], P. Hoeflich[2], E. Baron[3,4], M. Shahbandeh[5], B. J. Shappee[6], J. Andrews[7], D. Baade[8],
E. F Balangan[2], K. A. Bostroem[9,31], P. J. Brown[10], C. R. Burns[11], A. Burrow[12], A. Cikota[13], T. de Jaeger[6],
A. Do[6], Y. Dong[14], I. Dominguez[15], O. Fox[5], L. Galbany[16,17], E. T. Hoang[18], E. Y. Hsiao[2], D. Janzen[19],
J. E. Jencson[20], K. Krisciunas[10], S. Kumar[2], J. Lu[2], M. Lundquist[21], T. B. Mera Evans[2], J. R. Maund[22],
P. Mazzali[23,24], K. Medler[23], N. E. Meza Retamal[18], N. Morrell[25], F. Patat[8], J. Pearson[9], M. M. Phillips[25],
M. Shrestha[9], S. Stangl[12], C. P. Stevens[1], M. D. Stritzinger[26], N. B. Suntzeff[10], C. M. Telesco[27],
M. A. Tucker[28,32], S. Valenti[14], L. Wang[29], and Y. Yang[30,33]

[1] Department of Physics, Virginia Tech, Blacksburg, VA 24061, USA; jmderkacy@vt.edu
[2] Department of Physics, Florida State University, 77 Chieftan Way, Tallahassee, FL 32306, USA
[3] Planetary Science Institute, 1700 East Fort Lowell Road, Suite 106, Tucson, AZ 85719-2395, USA
[4] Hamburger Sternwarte, Gojenbergsweg 112, D-21029 Hamburg, Germany
[5] Space Telescope Science Institute, 3700 San Martin Drive, Baltimore, MD 21218-2410, USA
[6] Institute for Astronomy, University of Hawai'i at Manoa, 2680 Woodlawn Drive, Hawai'i, HI 96822, USA
[7] Gemini Observatory/NSFs NOIRLab, 670 North A'ohoku Place, Hilo, HI 96720-2700, USA
[8] European Organization for Astronomical Research in the Southern Hemisphere (ESO), Karl-Schwarzschild-Str. 2, D-85748 Garching b. München, Germany
[9] Steward Observatory, University of Arizona, 933 North Cherry Avenue, Tucson, AZ 85721-0065, USA
[10] George P. and Cynthia Woods Mitchell Institute for Fundamental Physics and Astronomy, Texas A&M University, Department of Physics and Astronomy, College Station, TX 77843, USA
[11] Observatories of the Carnegie Institution for Science, 813 Santa Barbara Street, Pasadena, CA 91101, USA
[12] Homer L. Dodge Department of Physics and Astronomy, University of Oklahoma, 440 W. Brooks, Rm 100, Norman, OK 73019-2061, USA
[13] Gemini Observatory/NSF's NOIRLab, Casilla 603, La Serena, Chile
[14] Department of Physics, University of California, 1 Shields Avenue, Davis, CA 95616-5270, USA
[15] Universidad de Granada, E-18071, Granada, Spain
[16] Institute of Space Sciences (ICE, CSIC), Campus UAB, Carrer de Can Magrans, s/n, E-08193 Barcelona, Spain
[17] Institut dEstudis Espacials de Catalunya (IEEC), E-08034 Barcelona, Spain
[18] Department of Physics and Astronomy, University of California, Davis, 1 Shields Avenue, Davis, CA 95616-5270, USA
[19] Department of Physics and Engineering Physics, University of Saskatchewan, 116 Science Place, Saskatoon, SK S7N 5E2, Canada
[20] Department of Physics and Astronomy, The Johns Hopkins University, 3400 North Charles Street, Baltimore, MD 21218, USA
[21] W.M. Keck Observatory, 65-1120 Māmalahoa Highway, Kamuela, HI 96743-8431, USA
[22] Department of Physics and Astronomy, University of Sheffield, Hicks Building, Hounsfield Road, Sheffield S3 7RH, UK
[23] Astrophysics Research Institute, Liverpool John Moores University, UK
[24] Max-Planck Institute for Astrophysics, Garching, Germany
[25] Las Campanas Observatory, Carnegie Observatories, Casilla 601, La Serena, Chile
[26] Department of Physics and Astronomy, Aarhus University, Ny Munkegade 120, DK-8000 Aarhus C, Denmark
[27] Department of Astronomy, University of Florida, Gainesville, FL 32611 USA
[28] Center for Cosmology and AstroParticle Physics, The Ohio State University, 191 W. Woodruff Avenue, Columbus, OH 43210, USA
[29] Department of Physics and Astronomy, Texas A&M University, College Station, TX 77843, USA
[30] Department of Astronomy, University of California, Berkeley, CA 94720-3411, USA

Abstract

We present a JWST mid-infrared (MIR) spectrum of the underluminous Type Ia Supernova (SN Ia) 2022xkq, obtained with the medium-resolution spectrometer on the Mid-Infrared Instrument (MIRI) $\sim$130 days post-explosion. We identify the first MIR lines beyond 14 μm in SN Ia observations. We find features unique to underluminous SNe Ia, including the following: isolated emission of stable Ni, strong blends of [Ti II], and large ratios of singly ionized to doubly ionized species in both [Ar] and [Co]. Comparisons to normal-luminosity SNe Ia spectra at similar phases show a tentative trend between the width of the [Co III] 11.888 μm feature and the SN light-curve shape. Using non-LTE-multi-dimensional radiation hydro simulations and the observed electron capture elements, we constrain the mass of the exploding WD. The best-fitting model shows that SN 2022xkq is consistent with an off-center delayed-detonation explosion of a near-Chandrasekhar mass WD ($M_{\rm WD} \approx 1.37\ M_\odot$) of high central density ($\rho_c \geqslant 2.0 \times 10^9$ g cm^{-3}) seen equator-on, which produced $M(^{56}{\rm Ni}) = 0.324\ M_\odot$ and $M(^{58}{\rm Ni}) \geqslant 0.06\ M_\odot$. The observed line widths are consistent with the overall abundance distribution; and the narrow stable Ni lines indicate little to no mixing in the central regions, favoring central ignition of subsonic carbon burning

---

[31] LSSTC Catalyst Fellow.
[32] CCAPP Fellow.
[33] Bengier-Winslow-Robertson Postdoctoral Fellow.

followed by an off-center deflagration-to-detonation transition beginning at a single point. Additional observations may further constrain the physics revealing the presence of additional species including Cr and Mn. Our work demonstrates the power of using the full coverage of MIRI in combination with detailed modeling to elucidate the physics of SNe Ia at a level not previously possible.

Unified Astronomy Thesaurus concepts: Supernovae (1668); Type Ia supernovae (1728); James Webb Space Telescope (2291)

1. Introduction

The use of Type Ia supernovae (SNe Ia) as cosmological distance indicators belies their diverse nature. Through the luminosity-width relation (Phillips 1993), both bright, slow-declining and dimmer, fast-declining SN Ia can be standardized for cosmological analyses, which have revealed the accelerating expansion of the universe (Riess et al. 1998; Perlmutter et al. 1999). Spectroscopic diversity among SNe Ia has also been observed, with multiple schemes to understand this diversity, based solely on spectroscopic information (Branch et al. 2006; Wang et al. 2009), or combined photometric and spectroscopic measurements (Benetti et al. 2005), having been developed. Evidence suggests that much of the observed diversity originates from differences in the radioactive Ni mass (e.g., ^{56}Ni; Nugent et al. 1995; Pinto & Eastman 2000a, 2000b), resulting in several subtypes of SNe Ia with unique photometric and spectroscopic properties including (but not limited to) the following: 91T-like objects (Filippenko et al. 1992b; Phillips et al. 1992, 2022; Yang et al. 2022), 91bg-like objects (Filippenko et al. 1992a; Leibundgut et al. 1993; Galbany et al. 2019; Hoogendam et al. 2022), 02cx-like objects (aka SN Iax; Li et al. 2003; Foley et al. 2013; Jha 2017), and 03fg-like objects (formerly known as super-Chandrasekhar SNe Ia; Howell et al. 2006; Hicken et al. 2007; Scalzo et al. 2010; Hsiao et al. 2020; Ashall et al. 2021).

A major outstanding question is whether individual SNe Ia subgroups (e.g underluminous or 91bg-like objects) arise from different progenitor systems and/or explosion mechanisms (or particular combinations thereof) than other subgroups. SNe Ia are known to originate from the thermonuclear explosion of a carbon-oxygen (C/O) white dwarf (WD) in a multistar system (Hoyle & Fowler 1960; Bloom et al. 2012). The range of possible progenitor systems includes the following: the single degenerate scenario in which the companion is a main-sequence star or an evolved, nondegenerate companion such as a red giant or He-star (Whelan & Iben 1973); the double degenerate (DD) scenario in which the companion is also a WD (Iben & Tutukov 1984; Webbink 1984), or a triple system in which at least two of the bodies are C/O WDs (Thompson 2011; Kushnir et al. 2013; Pejcha et al. 2013; Shappee & Thompson 2013).

Within the context of the above progenitor scenarios, multiple explosion mechanisms exist (e.g., Benz et al. 1990; Hoeflich & Khokhlov 1996; Rosswog et al. 2009; Pakmor et al. 2012; Kushnir et al. 2013; Pakmor et al. 2013; Soker et al. 2013; García-Berro et al. 2017; Lu et al. 2021). Currently, two of the leading explosion models are the detonation of a sub-M_{Ch} WD or the explosion of a near-M_{Ch} WD. In sub-M_{Ch} explosions, He on the WD surface (which may be accreted from a degenerate or nondegenerate companion) detonates, driving a shockwave into the WD, which triggers a second, interior detonation, which disrupts the whole WD (Nomoto et al. 1984; Woosley & Weaver 1994; Livne & Arnett 1995; Hoeflich & Khokhlov 1996; Shen et al. 2018; Polin et al. 2019;

Boos et al. 2021). In contrast, for near-M_{Ch} explosions, H, He, and/or C material is accreted from a companion star (which may again be degenerate or nondegenerate) onto the surface of the WD, until compressional heating triggers an explosion near the WD center (Nomoto et al. 1976; Iben & Tutukov 1984; Hoeflich & Khokhlov 1996; Diamond et al. 2018). The flame front may propagate as either a deflagration, detonation, or both via a deflagration-to-detonation transition (DDT; Khokhlov 1991; Hoeflich & Khokhlov 1996; Gamezo et al. 2003; Poludnenko et al. 2019).

Nebular-phase spectra of SNe Ia in the mid-infrared (MIR) are key to distinguishing between different explosion models. As the location of the photosphere is wavelength-dependent, different spectral lines are revealed in the MIR (Meikle et al. 1993; Höflich et al. 2002; Wilk et al. 2018), which are better at constraining the physics of SN explosions than their optical counterparts (Diamond et al. 2015, 2018). For example, the amount of stable Ni (e.g., ^{58}Ni) and other iron group elements (IGEs) serve as a direct indicator of the central density (ρ_c) at the time of explosion (Hoeflich & Khokhlov 1996; Seitenzahl & Townsley 2017; Blondin et al. 2022). Optical lines from stable Ni are only identified as weak components of heavily blended features (Maguire et al. 2018; Mazzali et al. 2020) and the 1.94 μm [Ni II] near-IR (NIR) line lies directly adjacent to (and often overlapping) a telluric region; making its identification difficult and sensitive to reduction methodology in high-quality data (Friesen et al. 2014; Dhawan et al. 2018; Diamond et al. 2018; Hoeflich et al. 2021). However, in the MIR, stable Ni can be seen even in low signal-to-noise ratio (S/N) observations (Gerardy et al. 2007; Telesco et al. 2015), with multiple strong lines in different ionization stages seen in high S/N JWST observations (Kwok et al. 2023a; DerKacy et al. 2023).

To date, the complete published sample of MIR nebular-phase spectra of SNe Ia contains nine spectra of five normal-luminosity objects,[34] and one spectrum of a 2003fg-like SNe Ia. This data includes single epoch observations of SNe 2003hv, 2005df (Gerardy et al. 2007), and 2006ce (Kwok et al. 2023a) with the Spitzer Space Telescope; plus a JWST observation of the 03fg-like SN 2022pul (Kwok et al. 2023b; Siebert et al. 2024). Two time series data sets exist; four observations of SN 2014J with CarnariCam on the Gran Telescopio de Canarias (Telesco et al. 2015), and two observations of SN 2021aefx (Kwok et al. 2023a; DerKacy et al. 2023) with the Low Resolution Spectrograph (LRS; Kendrew et al. 2015; Rigby et al. 2023) mode of the Mid-Infrared Instrument (MIRI; Rieke et al. 2015, and references therein). All of these published MIR spectra have resolutions of $R \lesssim 200$. With an average resolution $R \sim 2700$ from 5 to 25 μm, observations of SNe Ia with JWST/MIRI using the Medium Resolution Spectrograph (MRS; Rieke et al. 2015; Wells et al.

---

[34] We note that Leloudas et al. (2009) found SN 2003hv was a normal-luminosity SN Ia that obeys the Phillips relation, with $M(B) = -19.13$ mag, and $\Delta m_{15}(B) = 1.61 \pm 0.02$ mag.

Table 1
Properties of SN 2022xkq and NGC 1784

Parameter	Value	Source
SN 2022xkq		
R.A.	$05^h05^m23\overset{s}{.}70$	(1)
Decl.	$-11°52'56\overset{''}{.}13$	(1)
Last Nondetection (MJD)	59864.25	(1)
Discovery (MJD)	59865.37	(1)
t_{exp} (MJD)	59865.0 ± 0.3	(2)
t_{max} (MJD)	59879.03 ± 0.34	(2)
$M_{B,max}$ (mag)	-18.01 ± 0.15	(2)
$\Delta m_{15}(B)$ (mag)	1.65 ± 0.03	(2)
s_{BV}	0.63 ± 0.03	(2)
$E(B-V)_{MW}$ (mag)	0.116 ± 0.002	(3)
NGC 1784		
R.A.	$05^h05^m27\overset{s}{.}10$	(4)
Decl.	$-11°52'17\overset{''}{.}50$	(4)
Morphology	SB(r)c	(4)
v_{helio} (km s^{-1})	2291 ± 11	(5)
v_{rot} (km s^{-1})	41 ± 20	(4)
z	0.0077	(5)
μ	32.46 ± 0.15	(2)

Note. Pearson et al. (2024) find negligible host extinction at the site of SN 2022xkq.
References. (1) Janzen et al. (2022), (2) Pearson et al. (2024), (3) Schlafly & Finkbeiner (2011), (4) Ratay (2004), (5) Koribalski et al. (2004), and (6) NED (http://ned.ipac.caltech.edu/).

2015; Argyriou et al. 2023) can make more precise measurements of the line velocities and line profiles, and provide coverage in the 14–25 μm region unobtainable with MIRI/LRS. To date, no spectral observations of SNe Ia from MIRI/MRS have been published in literature.

In this work, we present a medium-resolution nebular-phase spectrum of the underluminous SN 2022xkq taken ∼ 130 days after explosion with MIRI/MRS. Section 2 describes our observations and reduction procedures. Line identifications are made in Section 3, and important aspects of the spectrum are characterized in Section 4, including discussions of the differences in the MIR spectra of SN 2022xkq versus normal-luminosity SNe Ia observed at similar epochs. We interpret these observations with the use of radiative hydrodynamic models, which are presented in Section 5. We summarize our results in Section 6 and discuss the implications of this work in Section 7. We conclude in Section 8.

2. Observations

2.1. Early Observations of SN 2022xkq

SN 2022xkq was discovered on 2022 October 13.4 UT (MJD = 59865.4) by the Distance Less Than 40 Mpc Survey (DLT40; Tartaglia et al. 2018), with a last nondetection on 2022 October 12.3 UT (MJD = 59864.3). Initially classified as a Type I (Chen et al. 2022a) or Type Ic (Hosseinzadeh et al. 2022) SN, further observations revealed SN 2022xkq to be a 91bg-like SN Ia (Chen et al. 2022b).

A detailed analysis of SN 2022xkq can be found in Pearson et al. (2024). We briefly summarize some of their key findings, with important measurements of SN 2022xkq and its host

NGC 1784 shown in Table 1. SN 2022xkq is a transitional SNe Ia similar to SNe 1986G (Phillips et al. 1987; Ashall et al. 2016b), 2005ke (Patat et al. 2012), 2007on, 2011iv (Ashall et al. 2018; Gall et al. 2018), and 2012ij (Li et al. 2022). SNooPy (Burns et al. 2011, 2014) fits to the early light curve show that SN 2022xkq has $\Delta m_{15}(B) = 1.65 \pm 0.03$ mag, and $s_{BV} = 0.63 \pm 0.03$. Using Arnett's Rule (Arnett 1982; Arnett et al. 1985), the pseudo-bolometric light curves, and the peak bolometric luminosity, Pearson et al. (2024) derived a ^{56}Ni mass of $0.22 \pm 0.03\,M_{\odot}$ in SN 2022xkq. Early photometry revealed SN 2022xkq to be red in color, with a flux excess in the redder bands relative to power-law fits in the first few days after explosion. In addition, densely sampled spectra showed strong, persistent C lines (particularly C I $\lambda1.069$ μm), similar to SN 1999by. Radio observations taken on 2022 October 15.9 with the Australia Telescope Compact Array (ATCA) found no radio emission at the site of SN 2022xkq, placing 3σ upper limits of 0.07 mJy at 5.5 GHz and 0.04 mJy at 9.0 GHz (Ryder et al. 2022).

The host galaxy of SN 2022xkq is NGC 1784, a barred spiral SB(r)c galaxy at a distance of roughly 31 Mpc (de Vaucouleurs et al. 1991; Pearson et al. 2024). SN 2022xkq is located near the edge of a weak spiral arm, 49$\overset{''}{.}$91 W and 38$\overset{''}{.}$63 S of the center of its host galaxy (see Figure 1 in Pearson et al. 2024). Underluminous SNe Ia are typically found in older stellar populations, and thus more likely to occur in elliptical galaxies (Branch et al. 1996; Hamuy et al. 1996; Howell 2001; Sullivan et al. 2010; Ashall et al. 2016a; Nugent et al. 2023); although old stellar populations can also be found in late-type spirals such as NGC 1784. Interestingly, the underluminous SN 1999by was also discovered in a late-type spiral (Howell 2001; Höflich et al. 2002; Garnavich et al. 2004), and shows some properties similar to those of SN 2022xkq (Pearson et al. 2024). NGC 1784 has a systemic recessional velocity of 2291 ± 11 km s^{-1} (Koribalski et al. 2004), when corrected for the influences of the Virgo Cluster, the Great Attractor, and the Shapley Supercluster (Mould et al. 2000). Detailed H I mapping of NGC 1784 reveals an implied rotational velocity of 41 ± 20 kms at the site of SN 2022xkq (Ratay 2004). Throughout this work, spectra have been corrected for the combined line-of-sight velocity (recessional plus rotational) of 2332 ± 23 km s^{-1} ($z = 0.007773 \pm 0.000077$). The H I maps also reveal a warped disk.

2.2. JWST Observations

SN 2022xkq was observed on 2023 February 19.0 by JWST with the Mid-Infrared Instrument (MIRI;Rieke et al. 2015) and Medium Resolution Spectrograph (MRS) as part of program JWST-GO-2114 (PI: C. Ashall). Full details of our observational setup can be found in Table 2. Observations began at 2023 February 19 00:30:30 UT (MJD = 59994.02) and ended at 2023 February 19 04:06:28 UT (MJD = 59994.17). Throughout this work, we adopt the midpoint of the observations (MJD = 59994.1), as the epoch of our observations, equivalent to 114.2 rest-frame days after B-band maximum (MJD = 59879.03) and 128.1 rest-frame days after explosion (MJD = 59865.0; Pearson et al. 2024).

Based on the in-flight performance report from Argyriou et al. (2023), MIRI/MRS is accurate to 2–27 km s^{-1} depending on wavelength, and has a spectrophotometric precision of 5.6%. The corresponding values for MIRI/LRS observation are 0.05–0.02 μm; corresponding to errors of ∼1400–500 km s^{-1},

Table 2
JWST MIRI/MRS Observation Details

Parameter	Value	Value	Value
	MIRI Acquisition Image		
Filter	F1000W	⋯	⋯
Acq. groups per exp.	10	⋯	⋯
Exp. time (s)	28	⋯	⋯
Readout pattern	FAST	⋯	⋯
	MIRI/MRS Spectra		
Wavelength range	Short	Medium	Long
Groups per integration	36	36	36
Integrations per exp.	1	1	1
Exposures per dither	1	1	1
Total dithers	4	4	4
Exp. time (s)	3440.148	3440.148	3440.148
Readout pattern	SLOWR1	SLOWR1	SLOWR1
T_{obs} [MJD]		59994.1	
Epoch[a] [days]		114.2	

Note.
[a] Rest-frame days relative to time of B-band maximum (MJD = 59879.03; Pearson et al. 2024).

again dependent on wavelength (DerKacy et al. 2023), and a spectrophotometric precision of ∼2%–5% (Kwok et al. 2023a).

2.3. JWST Data Reduction

The data were reduced using a custom-built pipeline[35] designed to extract point-source observations with a highly varying and/or complex backgrounds from MRS data cubes. This pipeline is discussed in detail in Appendix A of M. Shahbandeh et al. (2023, in preparation). In short, the pipeline creates a master background based upon 20 different positions in the data cube. This master background is then subtracted from the whole data cube before the aperture photometry is performed along the data cube, using the EXTRACT1DSTEP in stage 3 of the JWST reduction pipeline. The reduction shown here utilized version 1.12.1 of the JWST Calibration pipeline (Bushouse et al. 2023) and Calibration Reference Data System files version 11.17.1. The resulting MIRI/MRS cube is shown in Figure 1, and the spectrum is shown in full in Figure 2. The raw data associated with this reduction can be found at doi:10.17909/kfvh-wb96. The extracted spectrum has been smoothed with spextractor (Burrow et al. 2020) channel-by-channel to properly account for the differences in resolution across the full MIRI/MRS wavelength coverage.

3. Line Identifications

To identify the lines present in our +114.2 days spectrum of SN 2022xkq, we are guided by lines previously identified in other MIR spectra of normal-luminosity SNe Ia, as well as using the full non-LTE radiation-hydrodynamic models of the underluminous SN 2022xkq presented in Section 5. The line identifications are presented by MIRI/MRS channel in Figure 3, with individual lines specified in Table 3. We only identify features strong enough to exceed a flux level of 5% of the maximum flux of the smoothed spectrum at $\lambda < 20$ μm, or 10% of the maximum flux in the channel the feature is

[35] https://github.com/shahbandeh/MIRI_MRS

found, whichever is greater. Weaker features at or slightly exceeding the threshold level are considered tentative identifications.

At this phase, the ejecta is not yet fully nebular; meaning there is a combination of both permitted lines, forbidden emission, and an underlying continuum to the spectrum, creating a pseudo-photosphere (see Section 5), seen previously in the analysis of both SNe 2005df and 2014J at similar epochs (Gerardy et al. 2007; Diamond et al. 2015; Telesco et al. 2015). This results in many of the features arising from a combination of blends as well as radiative transfer effects, making the identification of individual components difficult. Below, we discuss clear feature detections, but note that many weak lines have no cross sections. Work to determine these missing cross sections using the MRS spectra of SN 2021aefx in combination with detailed non-LTE simulations is in progress (C. Ashall et al. 2023, in preparation).

3.1. Channel 1 (4.9–7.65 μm)

Channel 1 is dominated by a large, complex, seemingly box-shaped profile near ∼7.0 μm, with more isolated peaks on either side. These isolated peaks are easily identified as [Ni II] 6.636, and [Ni III] 7.349 μm lines arising from stable [58]Ni present in the ejecta. Both peaks appear blueshifted relative to their rest wavelengths and are further explored in Section 4.

As seen in the top panel of Figure 3, the dominant box-like feature reveals several peaks. This feature is primarily due to the [Ar II] 6.985 μm line seen in other SNe Ia spectra, with additional weak peaks across the box-like profile matching [Ni II] 6.920, [Co I] 7.045, and [Co III] 7.103 μm lines. A shoulder on the red side of this feature likely arises from a blend of [Co I] 7.191 and 7.200 μm lines. The [Ni III] 7.349 μm line also shows a weak shoulder in its red wing, which is likely attributable to the quasi-continuum (Fesen et al. 2015; Hoeflich et al. 2023).

No other strong features are present in the channel. Hints of weak, broad features appear in the ∼5–6.5 μm region, but none are well-matched by known spectral lines. The broad feature spanning ∼5.8–6.1 μm may arise in part from a blend of [Ni I] 5.893 and [Ni II] 5.953 μm lines, but it is unclear how much of the flux is due to the emission from forbidden Ni lines. As such, we leave this feature unidentified in both Figure 3 and Table 3.

3.2. Channel 2 (7.51–11.7 μm)

Similar to Channel 1, Channel 2 is also dominated by a single prominent feature, with additional weak features spread across the channel. The strongest feature is the blended feature near 9.0 μm. This blend shows a strong blue peak at ∼8.9 μm, likely from [Ni IV] 8.945 μm with some contribution of [Ti II] 8.915 μm. This peak is blended with the central line of the feature, [Ar III] 8.991 μm. A secondary peak in the red at roughly ∼9.1 μm could be produced from [Ti II] 9.197 μm; however, due to the increased noise in this part of the feature, it may be more shoulder-like in appearance with stronger contributions from additional iron group elements and/or the quasi-continuum. Due to the combination of this blending and asymmetry in the feature, the exact profile of the [Ar III] 8.991 μm is difficult to determine requiring detailed
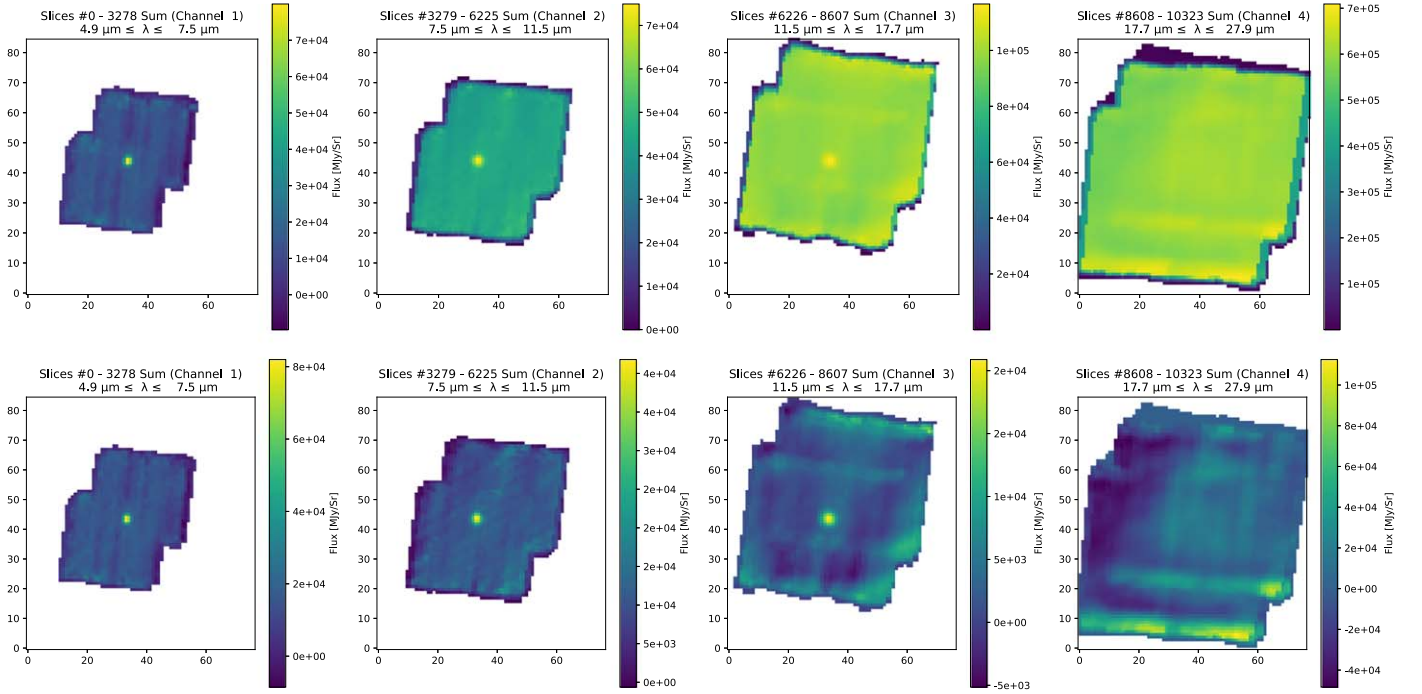
Figure 1. Top row: MIRI/MRS cube of SN 2022xkq before background subtraction, split into the four MIRI/MRS channels. The image shown for each channel is the collapsed sum of all its slices. Bottom row: MIRI/MRS cube of SN 2022xkq after background subtraction. We note that, although the SN cannot be seen in the stacked Channel 4 cube, it is visible in specific wavelength slices, as can be seen from the spectra in Figure 2.

models (e.g., Penney & Hoeflich 2014; Hoeflich et al. 2021), like in SN 2021aefx (Kwok et al. 2023a; DerKacy et al. 2023).

We tentatively identify some weaker features in Channel 2. The double-peaked feature from $\sim$8.2–8.4 μm is due to [Co I] 8.283, [Fe II] 8.299, and [Ni IV] 8.405 μm. A broad but weak blend is seen extending from roughly $\sim$10–11.4 μm, with contributions likely originating from [S IV] 10.511, [Ti II] 10.511, [Co II] 10.523, and [N II] 10.682 μm. A narrower, but equally weak feature exists between $\sim$11.1 and 11.4 μm, potentially arising from [Ni IV] 11.130, [Co II] 11.167, [Ti II] 11.238, and [Ni I] 11.307 μm lines.

Channel 2 terminates at roughly 11.7 μm, within the blue edge of the feature dominated by the [Co III] 11.888 μm resonance line. As the bulk of the feature is observed within Channel 3, we discuss the feature in the following section.

3.3. Channel 3 (11.55–18 μm)

Channel 3 begins in the blue wing of the [Co III] 11.888 μm blended feature. When examined as a whole, this feature is clearly dominated by [Co III] 11.888 μm, with the [Fe III] 11.978 and [Ni I] 12.001 μm lines making weaker contributions to the red shoulder, as previously seen in SN 2021aefx (DerKacy et al. 2023), with additional weak contributions due to [Ti II] 12.159 μm. Also similar to SN 2021aefx, a broad, multipeaked blend of weak features spanning $\sim$12.4–13 μm potentially results from [Fe II] 12.642, [Co III] 12.681, [Ni II] 12.729, and [Ne II] 12.811 μm lines (Blondin et al. 2023; DerKacy et al. 2023).

Beyond $\sim$14 μm, hints of strong features are seen between 14.6–15 and 15.6–16.8 μm. The former is likely the result of a complex of [Co II] 14.739, [Ni I] 14.814, and [Co II] 14.977 μm. In the latter, we identify the primary lines contributing to the main peak as [Co II] 16.152, 16.155, and 16.299, and [Co III]

16.391 μm. These are the first line identifications in this wavelength range for an SN Ia.

In much of the remaining parts of the channel, small peaks are seen at low significance and remain unidentified. Many of these peaks are expected to be contributions from weak iron-group lines with no measured cross sections. This is important for the astro-atomic physics community to address, with cross-validation between astronomical and atomic physics methods.

3.4. Channel 4 (17.7–27.9 μm)

We see a clear point source present in the SHORT subband of Channel 4 (17.70–20.95 μm). Between $\sim$18 and 19 μm, a broad, possibly multipeaked feature is discernible, arising from [Fe II] 17.936, [Ni II] 18.241, [Co I] 18.265, [Co II] 18.390, [S III] 18.713, [Co II] 18.804, [Fe II] 19.007, and [Fe II] 19.056 μm lines. In the MEDIUM and LONG subbands, the background becomes much more variable possibly due to the decreased sensitivity in Channel 4. This results in a likely undersubtraction, which appears as a growing continuum under the strong peaks. This continuum should not be interpreted as due to any physical process. Regardless of this, we see a clear point source in specific wavelength slices. Additionally, this continuum pushes the entire flux above the 10% strong line threshold, and to account for this uncertainty, we only tentatively identify lines associated with clear peaks and group them with the weak detections from Channels 1–3. Lines roughly corresponding to strong and/or broad peaks in the complex blends of the MEDIUM and LONG subbands include the following: [Fe III] 20.167, [Fe II] 20.928, [Ar III] 21.829, [Fe II] 20.986, [Ni I] 22.106 μm, a possibly blueshifted line of [Co IV] 22.800, [Fe II] 22.902, [Fe III] 22.925, [Ni II] 23.086, [Co II] 23.196, [Co IV] 24.040, [Fe I] 24.042, and [Co III] 24.070 μm. Relatively isolated peaks associated with [S I] 25.249, [Co II] 25.689, and [O IV] 25.890 μm are also tentatively
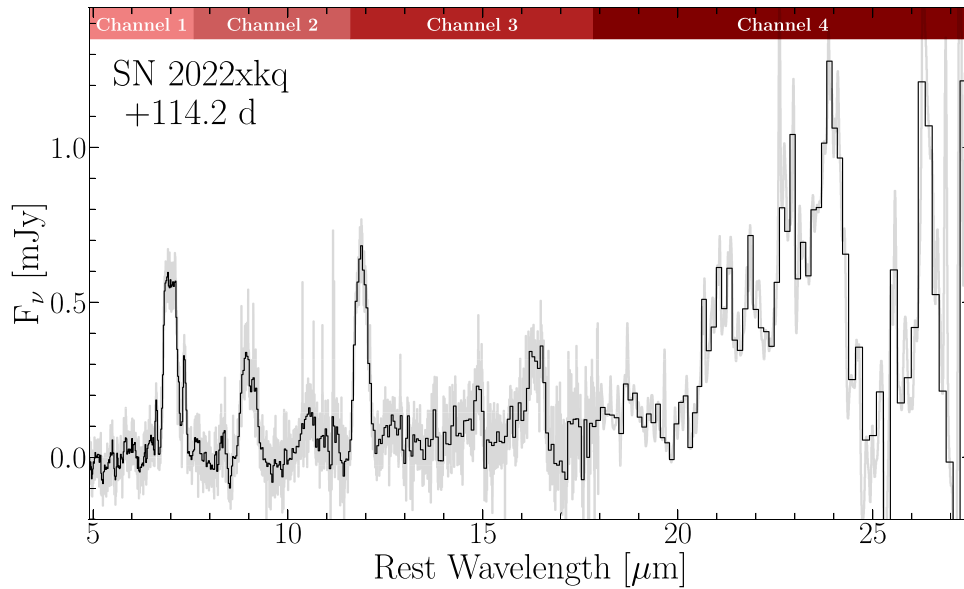
Figure 2. JWST MIRI/MRS observations of SN 2022xkq at +114.2 days relative to *B*-band maximum, corrected for Milky Way extinction. Raw data points are shown in gray, with the `Spextractor` (Burrow et al. 2020) smoothed spectrum in black. The channel labels at along the top axis are also corrected to the rest frame of the SN.

identified. As in Channel 3, many of the unidentified peaks likely correspond to weak iron-group lines lacking measured cross sections. Therefore, in order to obtain more information about which lines may be expected at $\lambda \gtrsim 21\ \mu$m and at what fluxes in underluminous SNe Ia, we turn to the models of synthetic spectra in Section 5.

4. Characterization of Underluminous SN Ia

Having identified the strong lines present in the MIR features of SN 2022xkq, we now attempt to measure the physical properties of these lines through spectral fitting. These fits allow us to estimate the central location and widths of the lines. However, due to line-blending, the complex physics of line formation at these epochs (see again Section 3 and later, Section 5), and the unknown strengths of many weak lines that produce the observed features in the spectrum, the resulting fits to most of the strong features in the spectrum are arbitrary with little physical meaning. By this, we mean that the peak of the fit, or its individual subcomponents, cannot be identified with any particular transition, and thus, it cannot directly probe the ejecta velocity.

Instead, we focus on fitting only those features that are relatively well isolated and result from lines with known cross sections, such as the [Ni II] 6.636, [Ni III] 7.349, and [Co III] 11.888 μm lines. For analysis of the more complex features, we take a data-only approach to estimating parameters from the features as a whole. The results of these measurements and their implications are discussed below.

4.1. Velocities of Isolated Lines

Among the strong features present in the observed spectrum of SN 2022xkq, only three are isolated enough with minimal blending to be fit with simple analytic functions. These features are those dominated by the [Ni II] 6.636, [Ni III] 7.349, and [Co III] 11.888 μm lines. In each case, the fits were performed using the modified trust-region Levenberg–Marquardt algorithm found in the `scipy.odr` package. Each spectral region

was fit with a Gaussian function with amplitude, mean, and standard deviation taken as free parameters. In order to better estimate the fit uncertainties, a Monte Carlo (MC) method was used to resample the spectrum (i.e., bootstrapping) and repeat the fit 500 times. The errors of the MC sample are then added to the known uncertainties of the data, such as spectral resolution, in quadrature to obtain the values presented below.

4.1.1. Stable Ni Lines

In all previously published MIR spectra of SNe Ia with the corresponding wavelength coverage, the [Ni II] 6.636 μm line has been either not detected (Gerardy et al. 2007) or identified as part of a blended feature (Kwok et al. 2023a, 2023b; DerKacy et al. 2023). In our MRS spectrum of SN 2022xkq, we see this feature as isolated and unblended—suggesting it should be representative of the stable Ni distribution within the core of the ejecta. Given the shape of the line profile, it is assumed that the emission is coming from a region of the ejecta, which has already reached the nebular state and can be modeled by a Gaussian function. However, it should be noted that fitting emission features with Gaussian profiles makes implicit assumptions about the nature of the line formation and spectral features (see Section 5), the underlying chemical distribution of ions within the ejecta, and should therefore be interpreted with caution. The resulting fit is shown in Figure 4, revealing a shift in the line center of $-460 \pm 110\ \mathrm{km\ s^{-1}}$, and an FWHM of $2460 \pm 110\ \mathrm{km\ s^{-1}}$.

Similarly, the [Ni III] 7.349 μm feature in SN 2022xkq is more isolated and unblended than in previous MIR observations of SNe Ia. However, compared to the [Ni II] 6.636 μm feature, fitting the [Ni III] feature requires more careful treatment. There is a significant contribution to the blue wing of the profile either from the continuum or an unknown weak line, and a weak shoulder in the red wing also due to unidentified lines. Neither wing component matches the known nebular lines near these wavelengths.

Initial attempts to fit the profile despite these complications yield a fit, which captures the width of the profile, but is unable
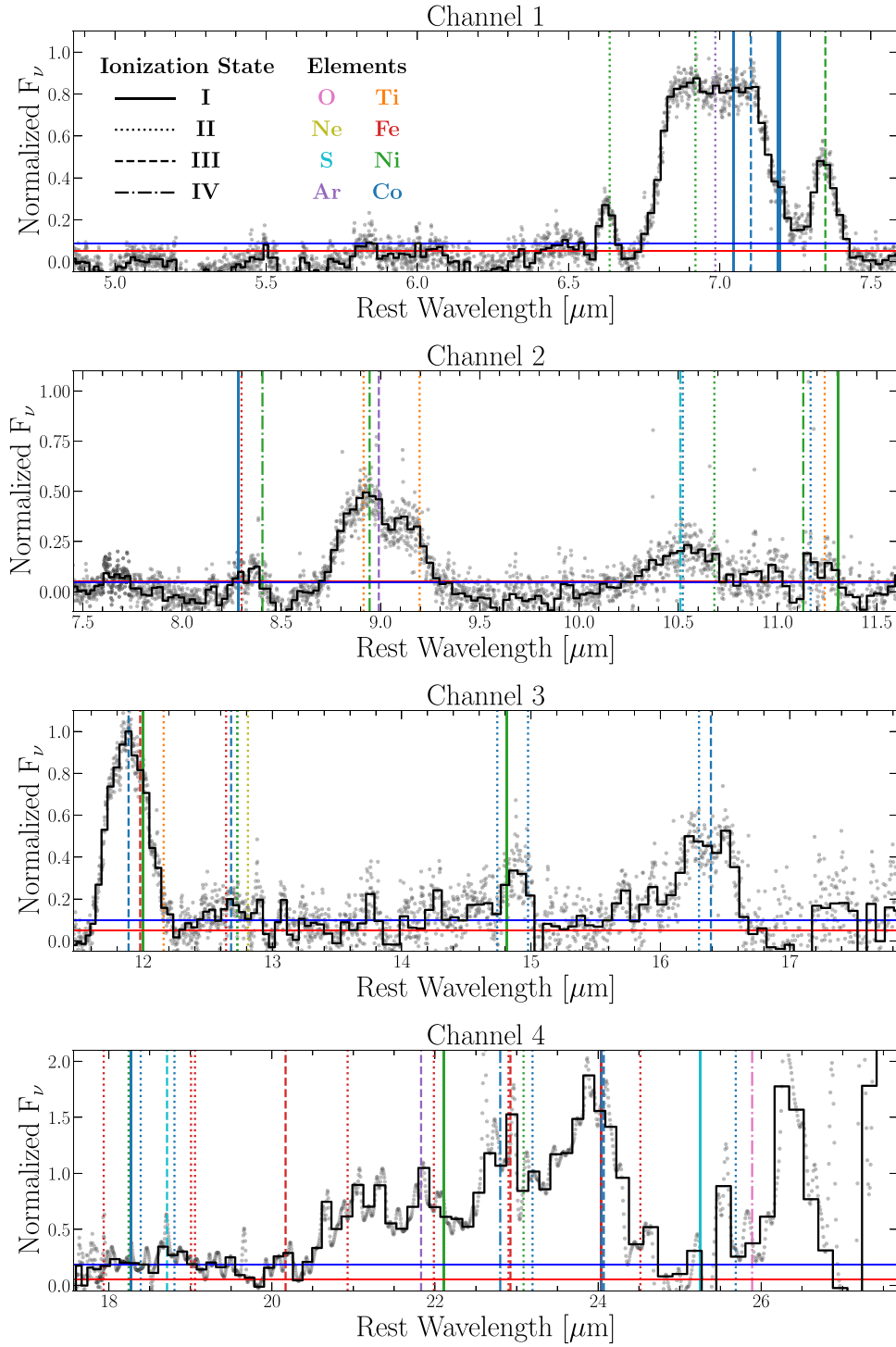
Figure 3. Spectrum of SN 2022xkq with line identifications based on known lines from previous MIR SNe Ia observations and models of underluminous SN Ia models. The horizontal lines denote the two threshold values of 5% of the overall flux (red) and 10% of maximum flux in each individual channel (blue); the larger of which must be exceeded for a feature to have line identifications.

to accurately measure the peak of the flux. Attempts to simultaneously account for potential contributions from the continuum and weak blending similarly capture the width of the feature, but are also unable to reproduce the correct location of the peak flux, and are strongly dependent on the choice of initial parameters defining the continuum.

Penney & Hoeflich (2014) have noted that, prior to the ejecta becoming optically thin through to the center, the locations of the peak fluxes will appear blueshifted relative to the true line center due to blocking of the red half of the line profile by the continuum, and that these effects are best measured after subtracting the continuum flux separately. After subtracting the continuum separately, the profile appears noticeably less Gaussian and requires at least a two Gaussian fit. The result of this fit captures the peak of the flux and width of the feature well; however, the assumed [Ni III] component is not the dominant line in the feature. Additionally, the strong component is not near the correct location to fit the weak blending in
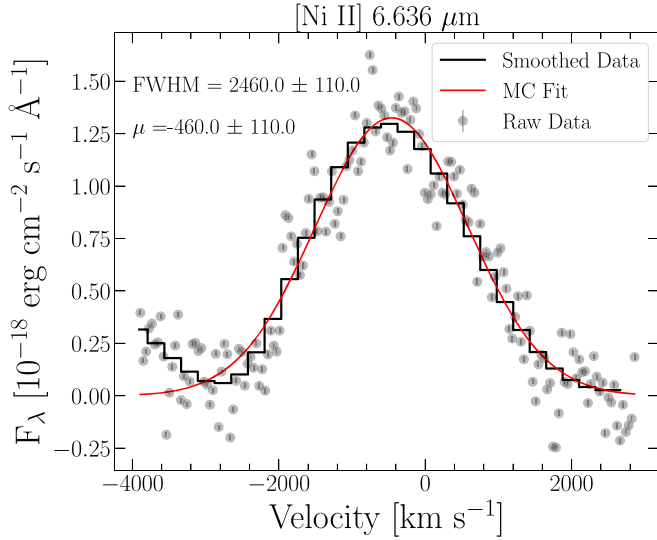
Figure 4. Single Gaussian MC fit to the [Ni II] 6.636 μm line. The best-fit parameters as determined from the MC results are: $\mu = -460 \pm 2$ km s^{-1}, and FWHM $= 2460 \pm 5$ km s^{-1}. The resolution error of 110 km s^{-1} dominates over both the uncertainties in the fit and in the wavelength calibration ($\sim$6 km s^{-1}; Argyriou et al. 2023).

the wings from the possible [Co I] lines. As there are no nearby lines resulting from ions commonly found in models of underluminous SN Ia, we regard the presence of an unidentified, strong line as unlikely.

Instead, we estimate the shift in the peak flux and the FWHM from a sample of 1000 bootstrapped resampled MC realizations of the spectra, assuming the flux errors are normally distributed. We find that the peak flux is shifted by -160 ± 140 km s^{-1}, with the FWHM of the feature measuring 3800 km s^{-1}. The results of this work are shown in Figure 5, and highlight the complexity of fitting even seemingly isolated and weakly blended features, and the effects of the photosphere present even during this late phase. Furthermore, Gaussian fits to complex features need to be interpreted with caution, as they fail to capture the physics of the line formation of these features, even at late times.

4.1.2. [Co III] 11.888 μm Feature

Resonance lines such as [Co III] 11.888 μm are important tracers of the amount and distribution of ions in the SN ejecta, since most of the deexcitation and recombination of each species will pass through their resonance transitions. Due to the decay chain of ^{56}Ni$\rightarrow$^{56}Co$\rightarrow$^{56}Fe, which powers the emission in SNe Ia, the [Co III] 11.888 μm feature serves as a late-time tracer of the initial ^{56}Ni distribution, which is located below the photosphere at early times. Previous low-resolution observations of the features dominated by [Co III] 11.888 μm have found that the line profiles are well-captured by a single Gaussian fit; however, spectral modeling reveals that up to $\sim$10% of the flux in the feature may result from weak blending with [Fe III] 11.978 and [Ni I] 12.001 μm lines in the red wing of the profile (Telesco et al. 2015; Kwok et al. 2023a; DerKacy et al. 2023).

In SN 2022xkq, the effects of the blending are clearly seen as a series of shoulders in the red wing of the profile in Figure 6 that are not present in the blue wing of the feature. However, much like the previous lower-resolution observations, the velocity shift, peak flux, and width of the feature are well-

Table 3
Line Identifications

| Line	λ (μm)	Line	λ (μm)	Line	λ (μm)
Lines in Strong Features					
[Ni II]	6.636	[Ni IV][a]	8.945	[Co II][a]	16.155
[Ni II][a]	6.920	[Ar II][a]	8.991	[Co II][a]	16.299
[Ar II][a]	6.985	[Ti II][a]	9.197	[Co III][a]	16.391
[Co I][a]	7.045	[Co III][a]	11.888	[Fe II][a]	17.936
[Co III][a]	7.103	[Fe III][a]	11.978	[Ni II][a]	18.241
[Co I][a]	7.191	[Ni I][a]	12.001	[Co I][a]	18.265
[Co I][a]	7.200	[Ni I][a]	14.814	[Co II][a]	18.390
[Ni III]	7.349	[Co II][a]	14.977	[S III][a]	18.713
[Ti II][a]	8.915	[Co II][a]	16.152	[Co II][a]	18.804
Lines in Weak Features					
[Co II][a]	8.283	[Fe III][a]	12.642	[Fe II][a]	22.902
[Fe II][a]	8.299	[Co III][a]	12.681	[Fe III][a]	22.925
[Ni II][a]	8.405	[Ni II][a]	12.729	[Ni II][a]	23.086
[S IV][a]	10.511	[Ne II][a]	12.811	[Co II][a]	23.196
[Ti II][a]	10.511	[Co II][a]	14.739	[Co IV][a]	24.040
[Co II][a]	10.523	[Co I][a]	15.936	[Fe I][a]	24.042
[Ni II][a]	10.682	[Fe III]	20.167	[Co III][a]	24.070
[Ni IV][a]	11.130	[Fe II][a]	20.928	[S I]	25.249
[Co II][a]	11.167	[Ar III][a]	21.829	[Co II]	25.689
[Ti II][a]	11.238	[Fe II][a]	20.986	[O IV]	25.890
[Ni I][a]	11.307	[Ni I][a]	22.106	⋯	⋯
[Ti II][a]	12.159	[Co IV][a]	22.800	⋯	⋯

Note.
[a] Denotes line is part of a blended feature.

represented by a single Gaussian fit, with the line center shifted by -170 ± 110 km s^{-1} and an FWHM of 8810 ± 110 km s^{-1}. As in the fits to the [Ni III] 6.636 μm line, the resolution error dominates over the statistical error of the fit. Comparisons between these fits in SN 2022xkq and the sample of other observed normal-luminosity SNe Ia are explored in further detail in Section 4.2. This highlights the need to approach Gaussian fits with caution, as the effects of blending are even stronger in the [Co III] 11.888 feature than in the [Ni III] 7.349 feature, despite the fact that a single Gaussian fit is sufficient to approximate the blended feature in this instance.

### 4.2. Underluminous versus Normal-luminosity SNe Ia MIR Spectra

4.2.1. Qualitative Comparisons

The published MIR sample of normal-luminosity SNe Ia is compared to our spectrum of SN 2022xkq in Figure 7. Four objects in the sample (SNe 2005df, 2006ce, 2014J, and 2022xkq) have MIR spectra taken roughly 120 days after B-band maximum light. These objects are directly compared in Figure 8, while key properties of each supernova can be found in Table 4.

The most prominent difference between the MIR spectrum of SN 2022xkq and the sample of normal-luminosity objects is the strength of the [Ar II] feature near 7 μm relative to the [Ar III] feature at $\sim$9 μm. These features are known to vary based on the geometry of the Ar distribution and viewing angle of the SN (Gerardy et al. 2007; DerKacy et al. 2023), although distinguishing these effects from continuum effects in spectra taken before the ejecta become fully nebular is much more
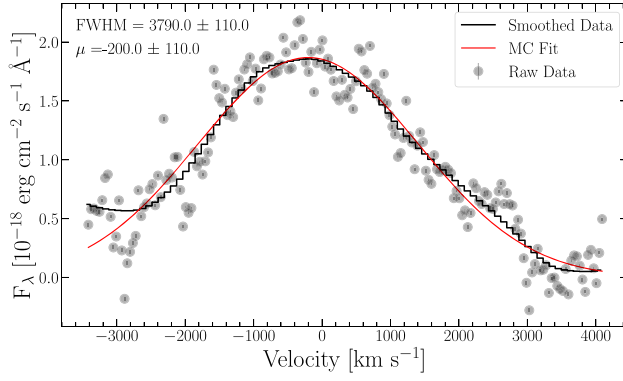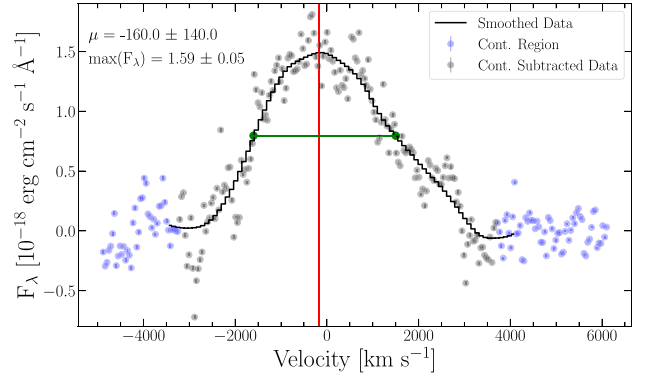
(a) Single Gaussian MC fit
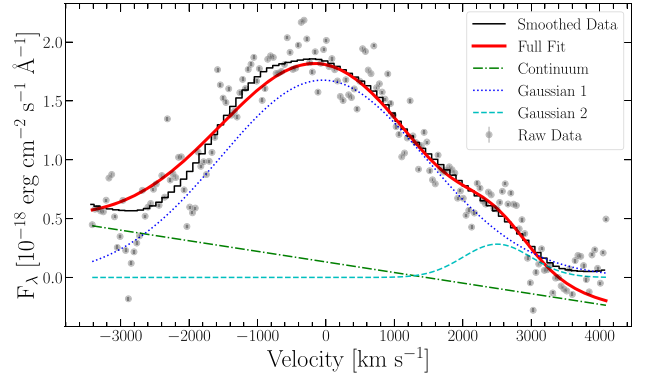

(b) Simultaneous multi-component fit
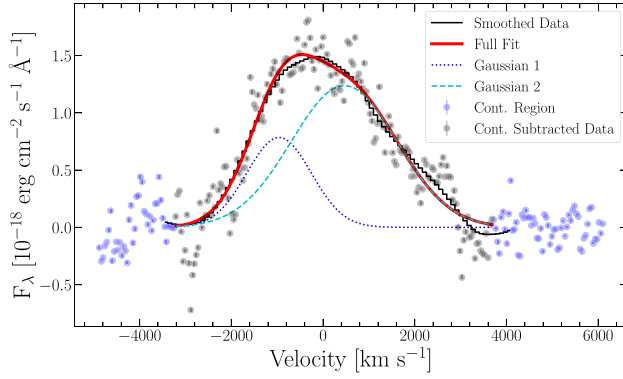
(c) Continuum-subtracted MC multi-Gaussian fit

(d) Continuum-subtracted data derived values

Figure 5. Fits to the [Ni III] 7.349 μm feature. Panel (a) shows the results of a single Gaussian fit similar to Figure 4. Panel (b) simultaneously fits the continuum component and multiple Gaussians, illustrating the non-Gaussianity of the feature. Panel (c) fits multiple Gaussian components after independently fitting and subtracting the continuum. Panel (d) shows the data derived values as measured from the continuum subtracted line profile.
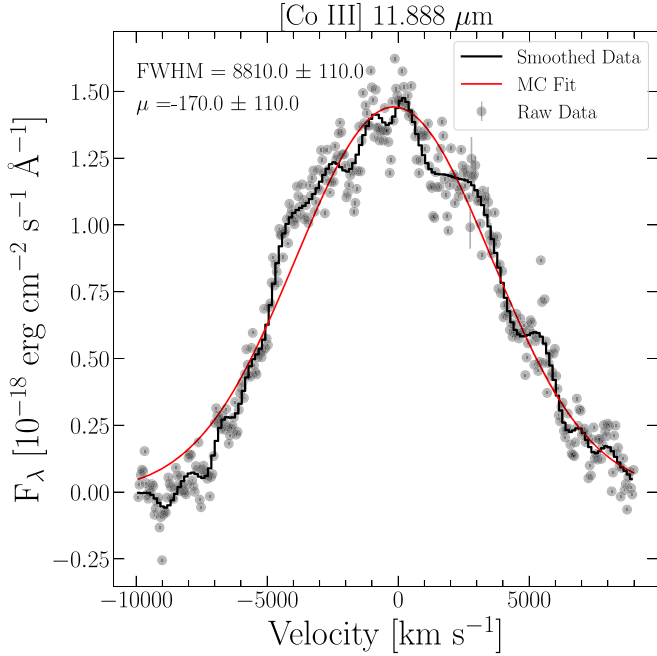

Figure 6. Same as Figure 4 but for the [Co III] 11.888 μm-dominated feature. The best-fit parameters determined from the MC ensemble are: $\mu = -170 \pm 5$ km s^{-1}, and FWHM $= 8810 \pm 5$ km s^{-1}. As before, the resolution error of ± 110 km s^{-1} dominates over the fit and wavelength calibration errors.

difficult. Yet, when comparing the line identifications in SN 2022xkq to those of the rest of the sample, we find the elements that dominate these features are similar, and produce prominent features in the same wavelength regions. The differences in the [Ar] lines are explored further in both Section 4.2.2 and Section 5.

Both the underluminous SN 2022xkq and the sample of normal-luminosity objects display weak, blended, broad features in the region between ∼10 and 11.5 μm (Figure 8). When compared to previous observations normalized to the peak of the [Co III] 11.888 μm resonance line, the relative flux in the features is similar. Spectra taken roughly 130 days after explosion have tentative identifications of [S IV] in combination with iron group elements (e.g., Fe, Co, and Ni) while the later spectra of SN 2021aefx only show the iron-group lines (Kwok et al. 2023a; DerKacy et al. 2023). The low spectral resolutions of previous observations make further direct comparisons difficult.

As expected, due to the underluminous nature of SN 2022xkq, the peak flux of the [Co III] 11.888 μm resonance line is significantly weaker than those in the other objects in the sample at similar epochs, all of which are normal-luminosity SN Ia (see the bottom panel of Figure 8). As a resonance line, the [Co III] 11.888 μm line directly traces the radioactive decay of the ^{56}Ni produced in the explosion through the ^{56}Ni→^{56}Co→^{56}Fe decay chain. The [Co III] line is also
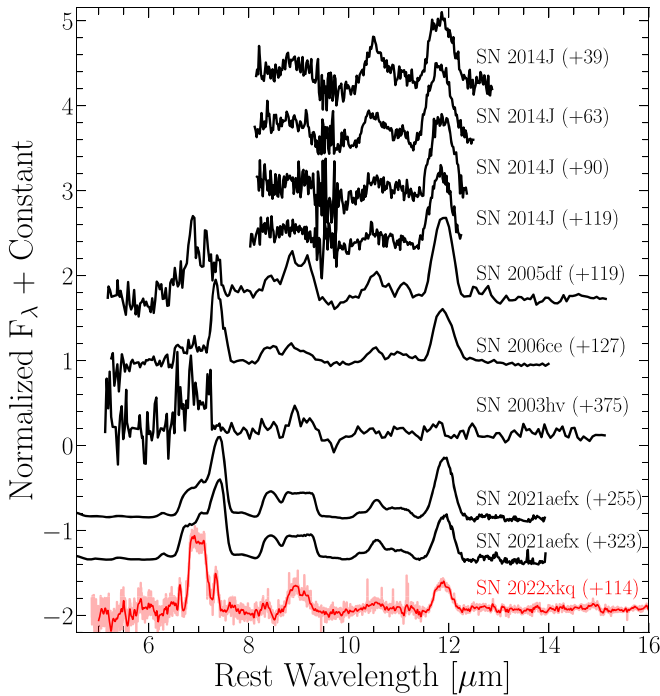
Figure 7. The published sample of normal-luminosity SNe Ia MIR spectral observations, including SNe 2003hv, 2005df (Gerardy et al. 2007), 2006ce (Kwok et al. 2023a), 2014J (Telesco et al. 2015), and 2021aefx (Kwok et al. 2023a; DerKacy et al. 2023). Epochs relative to B-band maximum are shown for each spectrum. For SN 2022xkq, a smoothed spectrum is shown in the foreground while the raw data is shown in the background. All spectra have been corrected for MW extinction.

noticeably narrower than the other normal-luminosity SNe Ia in the sample, consistent with measurements of the [Co III] 5890 Å in the optical (Graham et al. 2022). This behavior is also expected for underluminous SNe Ia, as nuclear burning occurs under lower density compared to normal SNe Ia resulting in lower ^{56}Ni production and a shift of nuclear burning products toward the inner, slower expanding layers. Moreover, more quasi-statistical equilibrium (QSE) elements are formed at the expense of nuclear statistical equilibrium (NSE) elements leading to increasing [Ar II/III] emission and narrower lines of all QSE and NSE elements (Höflich et al. 2002; Ashall et al. 2018; Mazzali et al. 2020). The differences in these [Co III] lines are quantified in Section 4.2.3.

4.2.2. Ar Lines

Figure 9 shows the region of the two prominent argon features, [Ar II] 6.985 and [Ar III] 8.991 μm, in SN 2022xkq compared to the same features in the subset of normal-luminosity SNe Ia spectra taken near 120 days after maximum light. For the normal-luminosity SNe Ia, it is difficult to ascertain the exact extent of the emission in velocity space due to a combination of low resolution and low S/N in the individual observations. However, for SN 2022xkq, it is clear that the wings of the emissions extend to $\sim$10,000 km s^{-1} in both argon dominated features. The ionization balance of SN 2022xkq is noticeably different than that of the other objects. In SN 2022xkq, the bulk of the argon is singly ionized, resulting in an average ratio of the peak flux of $\sim$2 between the [Ar II] and [Ar III] dominated features. In the normal-luminosity objects observed at similar epochs, this ratio is $\sim$1.

Furthermore, the total integrated flux in the Ar regions relative to the peak of the [Co III] is higher in SN 2022xkq, demonstrating that there is a larger argon abundance in the ejecta relative to the ^{56}Ni mass, as expected for an underluminous SN Ia (Ashall et al. 2018).

4.2.3. [Co III] 11.888 μm Profiles

Figure 10 shows the comparison of the [Co III] 11.888 μm features across the sample of MIR spectra taken $\sim$120 days after B-max. Compared to the lower-resolution observations with Spitzer (SNe 2005df, 2006ce) and CanariCam (SN 2014J) that smooth out much of the blending and continuum effects, the profile of SN 2022xkq is decidedly non-Gaussian. The blending effects primarily impact the red wings of the profile, with all four SNe showing similar full widths at zero-intensity (FWZI). These effects are not prominent in the blue wing, where the FWZI of SN 2022xkq at $\sim$7500 km s^{-1} is narrower than those of the normal-luminosity objects ($\gtrsim$10,000 km s^{-1}).

As a consequence of the [Co III] 11.888 μm resonance line being formed by the radioactive ^{56}Co in the ejecta, it serves as a direct tracer of the original distribution of ^{56}Ni in the explosion. As such, the width of the feature is characteristic of the burning conditions of the NSE region. As previously discussed above for underluminous SNe Ia, burning to ^{56}Ni occurs more centrally in the ejecta, which has the effect of producing a narrower [Co III] 11.888 μm feature.

Figure 11 shows the FWHM of this [Co III] 11.888 μm feature as a function of light-curve shape, $\Delta m_{15}(B)$. We see a rough trend between light-curve shape and width of the [Co III] 11.888 μm feature, where broader, more luminous SNe Ia have larger values of FWHM compared to the underluminous SN 2022xkq. As the sample of MIR spectra of SNe Ia increases, this figure can be populated with various types of SNe Ia to understand how closely the [Co III] 11.888 μm feature traces the luminosity of the SNe, allowing us to see how closely this plot follows the luminosity-width relation (Phillips 1993). A similar trend has been found through spectral modeling of the optical data (Mazzali et al. 1998, 2007), as well as in the [Co III] 5890 Å line in optical nebular spectra (Graham et al. 2022). While both the optical and MIR [Co III] lines are resonance lines, it is important to test this relation with the MIR line that is from a very low lying state from which the resonance transition is the only downward transition out of this low lying state. The more energetic upper state of the [Co III] 5890 Å transition, in addition to decaying to the ground state, also decays to the upper state of the MIR line. The optical line from this transition at 6190 Å is not a prominent feature in the spectra shown by Graham et al. (2022), nor are other nearby [Co III] resonance lines. There is also disagreement in the literature about whether the feature associated with [Co III] 5980 Å is due (in part) to Na I D (Kuchner et al. 1994; Mazzali et al. 1997; Dessart et al. 2014).

5. Modeling

We compare SN 2022xkq to new simulations of off-center M_{Ch} explosion models,[36] with parameters based upon the spherical models of the Model 16-series of Hoeflich et al. (2017). The early light-curve properties and maximum light luminosity of the models are very similar to that of

---

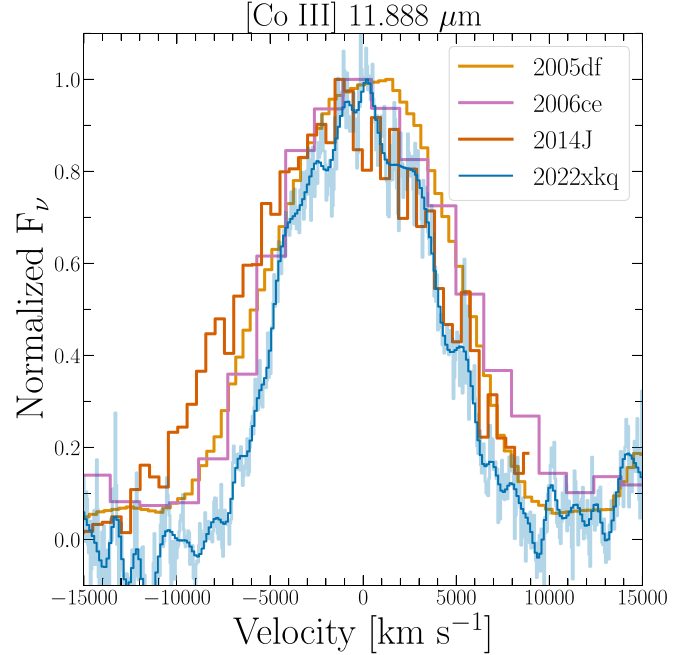[36] These simulations use the updated atomic models and MIR cross sections of C. Ashall et al. (2023 in preparation).
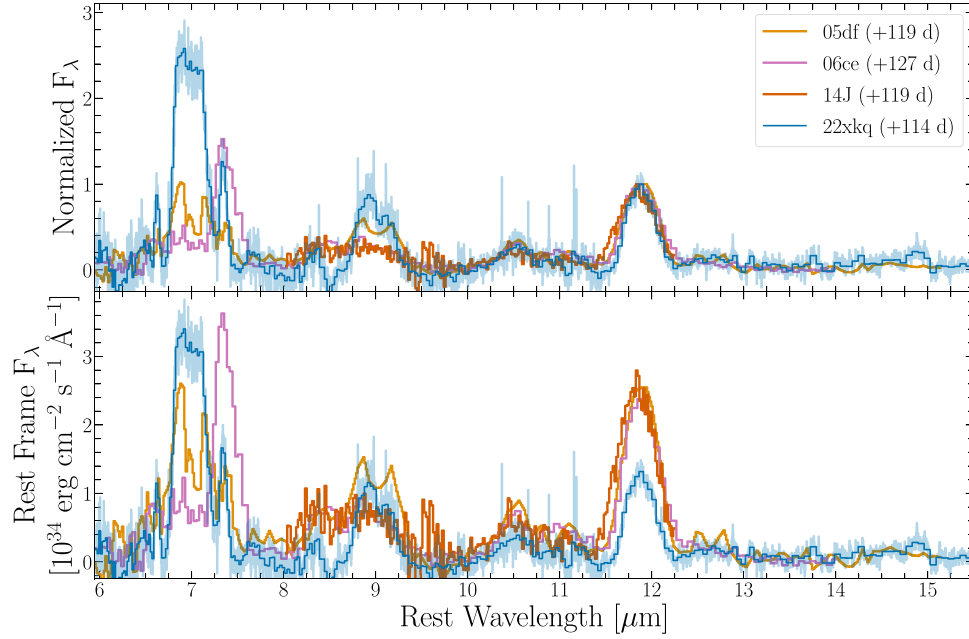
Figure 8. Comparison of SNe Ia spectra observed ∼120 days after maximum light in the MIR. The top panel shows flux values normalized to the peak of the [Co III] 11.888 μm features, while the bottom panel shows the fluxes corrected to the SN rest frame based on the estimated distances in Table 4. In SN 2022xkq, the singly ionized features (e.g., [Ni II] 6.636 μm and [Ar II] 6.985 μm) are stronger relative to their doubly ionized counterparts ([Ni III] 7.349 μm and [Ar III] 8.991 μm) as is expected in an underluminous SN Ia.
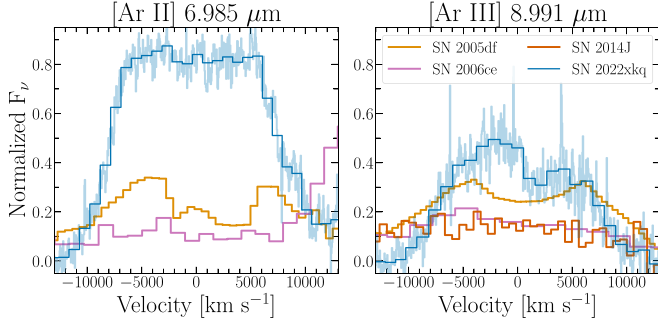
Figure 9. Comparison of Ar line profiles between SN 2022xkq and other normal-luminosity SNe Ia roughly 120 days after B-band max. As expected, the overall fluxes in the [Ar]-dominated features are larger in SN 2022xkq than in the normal-luminosity objects, while the increased strength of the [Ar II] feature relative to the [Ar III] feature in SN 2022xkq indicates that the ionization balance in the ejecta favors Ar II over Ar III (Gerardy et al. 2007; Ashall et al. 2018; Mazzali et al. 2020).

Figure 10. Same as Figure 9, but instead comparing the [Co III] 11.888 μm dominated features. The unblended blue wings of the profile reveal SN 2022xkq has a much narrower distribution of ^{56}Co relative to the normal-luminosity objects.

SN 2022xkq. No further fine-tuning of the basic parameters have been done, nor is it is necessary in light of uncertainties in distance and reddening. In order to move beyond profile fits, the synthetic spectra are modeled by detailed non-LTE radiation-hydrodynamic simulations, which link the observations to the underlying physics identify and quantify the contribution of specific transitions to observed spectral features. The observed features are dominated by a combination of emission lines, a quasi-continuum of allowed and forbidden lines in an envelope with varying element abundances, and strong non-LTE effects. We choose our best-fit model by comparing line profiles and line-ratios of noble gases like Ar and of electron capture elements such as Ni.

The simulations are parameterized explosion models, where we use the spherical delayed-detonation scenario to constrain the global parameters of the explosion. Fine-tuning these models is not necessary to achieve the goals of this study, as we

focus on spectra rather than high-precision photometry. The reference model (Figure 12) originates from a C/O WD with a main-sequence progenitor mass of 5 $M_{\odot}$, solar metallicity, and a central density $\rho_c = 2.0 \times 10^9$ g cm^{-3}. The model produces ∼0.324 $M_{\odot}$ of ^{56}Ni. The resulting light curves have a peak brightness of $M(B) = -18.22$ mag, and $M(V) = -18.37$ mag, and light-curve decline rates of $\Delta m_{15}(B) = 1.67$ mag, and $\Delta m_{15}(V) = 1.18$ mag. These can be compared to $M(B) = -18.1 \pm 0.15$ mag, and $\Delta m_{15}(B) = 1.65 \pm 0.03$ mag

Table 4
Properties of SNe Ia with MIR Spectra at ~120 Days

| Parameter	SN 2005df	SN 2006ce	SN 2014J	SN 2022xkq
Epoch (days)	119	127	119	114.2
$M_{\mathrm{B,peak}}$ (mag)	-19.27 ± 0.31	⋯	-19.19 ± 0.10	-18.01 ± 0.15
$\Delta m_{15}(B)$ (mag)	1.12[a]	⋯	1.12 ± 0.02	1.65 ± 0.03
s_{BV}	0.95[b]	⋯	0.95[b]	0.63
d (Mpc)	19.8 ± 2.8	19.6 ± 2.87	3.4 ± 0.1	31.0 ± 2.0

Notes. No optical photometry of SN 2006ce is publicly available.
[a] No error reported.
[b] Value calculated from $\Delta m_{15}(B)$ according to Equation (4) of Burns et al. (2014).
References. SN 2005df: Takáts et al. (2015), Krisciunas et al. (2017). SN 2006ce: Kwok et al. (2023a), NED. SN 2014J: Marion et al. (2015). SN 2022xkq: Pearson et al. (2024), this work.
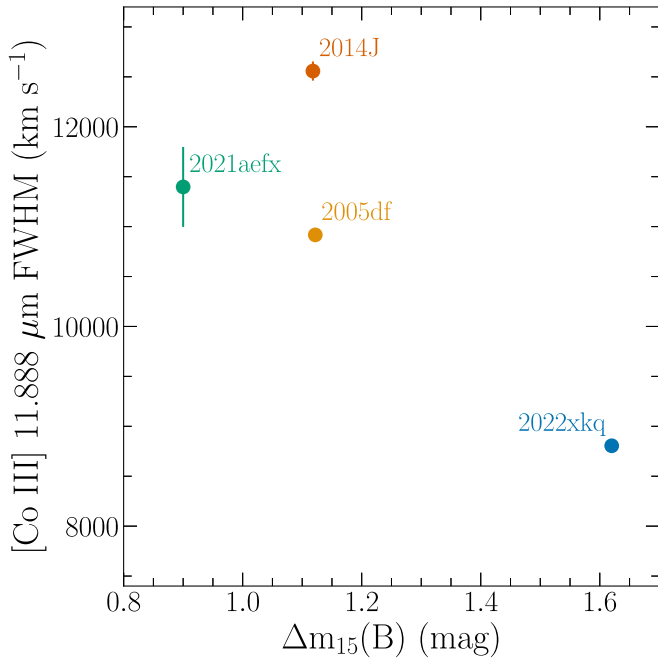
Figure 11. [Co III] 11.888 μm FWHM vs. $\Delta m_{15}(B)$ for SNe Ia with detected [Co III] emission and well-characterized light curves. We include the value from SN 2021aefx obtained at ~ + 323 days from the explosion (DerKacy et al. 2023), but note that this value may be uncertain due to the different physical regime in which the epoch is measured and potential line-blending.

obtained from the early time light curve (Pearson et al. 2024). The inferred absolute brightness at maximum light depends sensitively on the reddening, the distance modulus, and their uncertainties. Pearson et al. (2024) estimated a ^{56}Ni-mass of $0.22 \pm 0.03\,M_\odot$ compared to the $0.34\,M_\odot$ we obtain using nebular MIR spectra. Derived ^{56}Ni masses are uncertain, in particular for underluminous SNe Ia because the Q- or α-value in Arnett's law varies from 0.8 to 1.6 over a small brightness range, and similar differences occur among various methods (Höflich et al. 2002; Stritzinger et al. 2006; Hoeflich et al. 2017). The value of the ^{56}Ni mass obtained here is consistent with that of Pearson et al. (2024) within the errors.

Our value of ρ_c is chosen based upon the presence of stable Ni lines and to match the ionization balance in the observed MIR spectrum (see Figure 3 and Section 5.2.1). Burning starts as a deflagration front near the center and transitions to a detonation (Khokhlov 1991). The DDT is triggered by

increasing the rate of burning by the Zeldovich-mechanism (Zel'dovich 1940; von Neumann 1942; Döring 1943), that is, the mixing of burned and unburned material. Various mechanisms have been suggested to initiate the DDT transition, ranging from mixing by turbulence, shear flows at chemical boundaries, and differential rotation in the WD. Moreover, the mixing may depend on the conditions during the thermonuclear runaway (Khokhlov et al. 1997a; Livne 1999; Bell et al. 2004; Yoon et al. 2004; Höflich 2006; Charignon & Chièze 2013; Hristov et al. 2018; Poludnenko et al. 2019; Brooker et al. 2021). Although the recently suggested mechanism of turbulent-driven DDT in the distributed regime of burning (Oran 2011; Poludnenko et al. 2019) is consistent with the amount of deflagration burning in our parameterized models (Höflich et al. 2002; Hoeflich et al. 2023), other DDT mechanisms may be realized. We evaluate constraints from the observations of SN 2022xkq, treating the location of the DDT as a free parameter.

In our simulations, the deflagration–detonation transition is triggered "by hand" when ~0.34 $M_\odot$ of the material has been burned by the deflagration front and is induced by the mixing of unburned fuel and hot ashes (Khokhlov 1991). Our simulations take into account magnetic fields for the positrons. However, at 130 days, the mean free path of positrons is small even for small initial magnetic fields (Penney & Hoeflich 2014). We assume $B = 10^6$ G based upon our prior modeling of light curves and late-time nebular spectra (Diamond et al. 2015; Hristov et al. 2021). We have examined models where ρ_c was varied from 0.5 to 4.0×10^9 g cm^{-3} in order to study the effect of the WD central density on the MIR spectra and conclude that $\rho_c = 2.0 \times 10^9$ g cm^{-3} best reproduces the observations. The flux changes by ~15% between models with our fiducial value and those with $\rho_c = 4 \times 10^9$ g cm^{-3}, because the photosphere masks the appearance of very neutron-rich isotopes. However, lower central densities radically change the spectra.

Following the central carbon ignition and the propagation of the deflagration front, the deflagration transitions to a detonation. Rather than assuming that the DDT occurs in a spherical shell, it is assumed to begin as an off-center point as described by Livne & Arnett (1995) and in our previous work (Penney & Hoeflich 2014; Fesen et al. 2015; Hoeflich et al. 2021; DerKacy et al. 2023; Hoeflich et al. 2023). The effective spectral resolution is $R \approx 300$–600 (Hoeflich et al. 2021). We constructed models where the off-center location for the delayed-detonation transition occurred at $M_{\mathrm{DDT,off}}$ of 0, 0.2, 0.5, and 0.9 $M_\odot$. For computational expediency, only the model
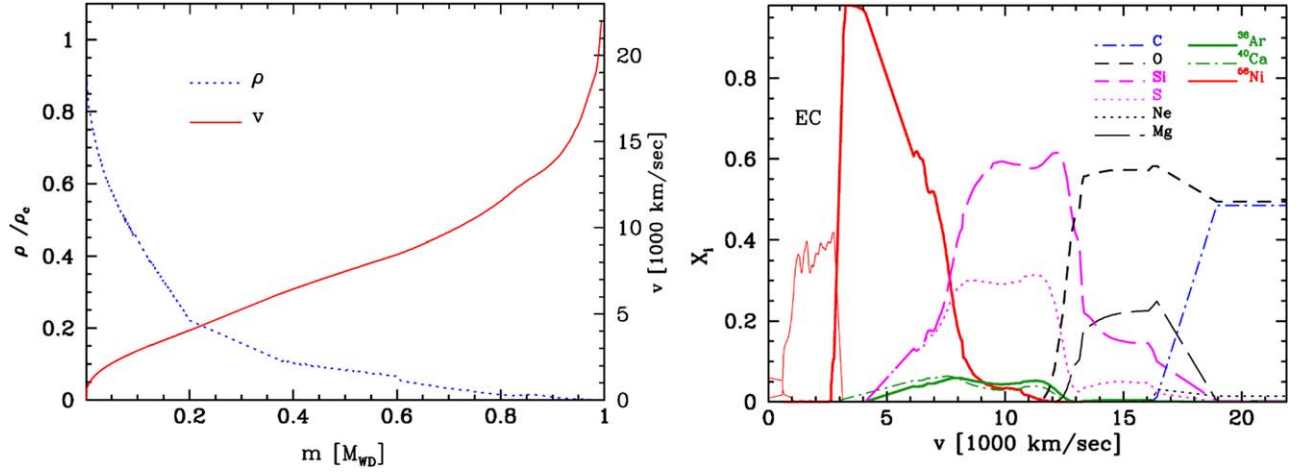
Figure 12. Density and velocity structure as a function of mass coordinate (left) and distribution of elements for our reference underluminous models with $\rho_c = 2 \times 10^9$ g cm^{-3}. Note that M_{DDT} was chosen to be 0.2 $M_\odot$. For the influence of ρ_c on the size electron capture core, see Diamond et al. (2015).

Table 5
Model Parameters and Light-curve Parameters for Various ρ_c

Parameter	Value	Value	Value	Value
ρ_c[$\times 10^9$ g cm^{-3}]	0.5	1.0	2.0	4.0
M_{ej} ($M_\odot$)	$\sim$1.37	$\sim$1.37	$\sim$1.37	$\sim$1.37
M_{tr} ($M_\odot$)	0.33	0.34	0.34	0.36
B(WD, turbulent) (G)	10^6	10^6	10^6	10^6
$M(B/V)$ (mag)	$-18.43/-18.57$	$-18.29/-18.46$	$-18.22/-18.37$	$-17.98/-18.06$
$\Delta m_{15}(B/V)$ (mag)	1.61/1.15	1.65/1.16	1.67/1.18	1.42/1.02
$B - V$ (V_{max}) (mag)	0.150	0.152	0.152	0.158

Note. The DDT is unlikely to occur between 0.3–0.5 $M_\odot$ because overlapping of the Ca-rich layers with the bulge of the ^{56}Ni would lead to a narrow [Ca II] doublet. The amount of mass burned during the deflagration M_{tr} includes both ^{56}Ni and EC elements.

with 0.2 $M_\odot$ has been fully converged with complex model atoms. Note that we use an off-center DDT in a single spot because it does not produce a refraction wave. Based on the discussion in Hoeflich et al. (2021), the almost flat top of the [Ar II] 6.985 μm feature suggests that SN 2022xkq is seen at a low inclination angle (θ) with $|\theta| \lesssim 20°$–30°. The absence of a narrow ($<$1000 km s^{-1} FWHM) [Ca II] $\lambda\lambda$7293, 7326 Å doublet in SN 2022xkq (Pearson et al. 2024) excludes that the DDT occurs close to the inner edge of the ^{56}Ni region, justifying a $M_{DDT} \approx 0.2$ $M_\odot$, or less. This is in contrast with our models for SN 2020qxp where the large overlap between Ca-rich region and NSE region results in a strong and narrow [Ca II] feature appearing $\sim$100 days after the explosion (see the inset of Figure 4 in Hoeflich et al. 2021),[37] regardless of the observation angle. Theoretically, a central DDT cannot be excluded because unburned material could be dragged down during the deflagration phase. However, the observed narrow ^{58}Ni features exclude a central DDT. The DDT is triggered by increasing the rate of burning by the Zeldovich-mechanism (Zel'dovich 1940; von Neumann 1942; Döring 1943). At the time of the DDT, the expansion of the inner electron capture region is subsonic (see, for example, Figures 9–10 in Hoeflich 2017). Thus, with an increased rate of burning and energy production, the buoyancy will mix the electron capture elements out to higher velocity, inconsistent with the observed

narrow ^{58}Ni lines. For the best-fitting model (Figure 12), we used an off-center DDT with $M_{DDT,off} = 0.2$ $M_\odot$ because we have no strong evidence for asymmetry from the line profiles, either because the observing angle is close to the equator or because the DDT is well inside of the Ca/Ar region. Stronger constraints would require later time observations in the optical to MIR. Nonetheless, off-center DDTs have been used to avoid the artifact of low-density burning due to the strong refraction wave evident in spherical simulations (Khokhlov et al. 1993; Hoeflich & Khokhlov 1996).

The non-LTE atomic models and the radiation transport used in this work were discussed in Hoeflich et al. (2021). Detailed atomic models are used for the ionization stages I-IV for C, O, Ne, Mg, Si, S, Cl, Ar, Ca, Sc, Ti, V, Cr, Mn, Fe, Co, Ni. As before, the atomic models and line lists are based on the database for bound-bound ($\approx$40,000,000 allowed and forbidden) transitions of van Hoof (2018)[38] supplemented by additional forbidden lines (Diamond et al. 2015), and lifetimes based on the analysis by our non-LTE models of SN 2021aefx (C. Ashall et al., 2023, in preparation).

5.1. Model Structure

The basic model parameters and light-curve observables are given in Table 5. The angle-averaged structure of the best-fitting model is shown in Figure 12. As expected for "classical" delayed-detonation models, the density and

---

[37] The simulations of SN 2022qxp were developed from the same base-model as SN 2022xkq but with different central densities (4×10^9 g cm^{-3}) and DDTs (0.5 $M_\odot$).

[38] Version v3.00b3 https://www.pa.uky.edu/~peter/newpage/.
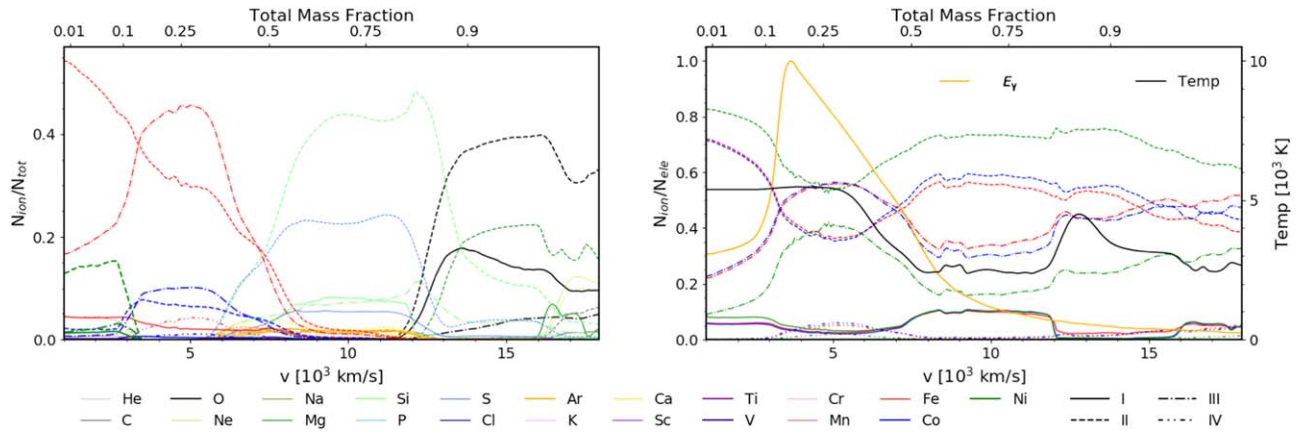
Figure 13. Same as the right panel from Figure 12 but angle-averaged ionization levels I–IV of Fe and Co as representative of iron-group elements, specific energy input by γ-rays and nonthermal leptons normalized to its maximum, and temperature T as a function of expansion velocity. Note that the overall ionization structure is rather insensitive to ρ_c because the shift in the balance is dominated by the recombination rate and, thus, the density. E_γ is dominated by γ-rays rather than positrons, which only is loosely correlated with the ^{56}Ni distribution. Namely, E_γ escape the outer layers, and we have significant heating in the core resulting in overall peaked line profiles of the iron group elements (see below and Figure 15).

velocity distributions are smooth (e.g without a shell) because the WD becomes unbound during the deflagration phase, in contrast to pulsating DD or pure deflagration models from Nomoto et al. (1984), Hoflich et al. (1995), Niemeyer & Woosley (1997), Bravo et al. (2009), and Hoeflich et al. (2017). Within the M_{Ch} scenario, a low luminosity/low ^{56}Ni mass is produced by an increased mass of deflagration burning, which leads to a larger pre-expansion of the WD and lower-density burning. Our model for SN 2022xkq falls into the $\Delta m_{15}(B/V)$ regime of rapidly dropping opacities soon after maximum light, a regime of fast-declining peak luminosity within a relatively narrow range of $\Delta m_{15}(B/V)$ (Höflich et al. 2002). This is similar to SN 1991bg-like objects (as indicated by the [Ti II] lines) and slightly more luminous than SN 2005ke or SN 2016hnk (Patat et al. 2012; Galbany et al. 2019). As a result, the models show unburned C/O, and products of explosive O-burning, and incomplete Si-burning layers down to $\approx$ 16,000, 12,000, and 5000 km s^{-1}, respectively. For M_{Ch} models of underluminous SNe Ia, the element production is shifted toward partial burned fuel corresponding to the following: $\sim$0.27–0.35 $M_\odot$ of $M(^{56}$Ni), $\sim$0.65 $M_\odot$ of intermediate mass elements (IMEs; Si and S), and $\sim$0.1 $M_\odot$ of unburned carbon (Höflich et al. 2002). In models of normal-luminosity SNe Ia, these values are 0.55–0.65 $M_\odot$, 0.2 $M_\odot$, and 1–2 × 10^{-2} $M_\odot$, respectively (Höflich et al. 2002). In our reference model, the layers expanding interior to $\approx$3000 km s^{-1} are dominated by electron capture elements, mostly ^{54}Fe, ^{57}Co, and ^{58}Ni.

The ionization structures at day 130 are shown in Figure 13. Overall, when compared to normal-luminosity SNe Ia (e.g., Wilk et al. 2020), the global ionization balances are shifted toward lower ionization states, as has also been shown for other underluminous SNe Ia, (Hoeflich et al. 2021). All the non-iron-group elements (e.g., C, O, Mg, Si, S, Ca) are dominated by singly ionized features, with significant contribution from neutral ions. For iron group elements, doubly ionized species dominate in the ^{56}Ni region, but the equilibrium is shifted toward single ionized species farther inwards due to the high densities. The region dominated by double ionized iron group elements in SN 2022xkq is absent in SN 2020qxp. A further difference between SN 2022xkq and SN 2020qxp is an extended region of singly ionized species in SN 2022xkq

rather than singly ionized species concentrated in the center. The difference between the transitional spectrum of SN 2022xkq and the nebular spectrum of SN 2020qxp obtained 190 days after explosion can be understood as due to the higher densities (in the ^{56}Ni region) and the energy input in SN 2022xkq that are dominated by non-local γ-ray heating. Positrons dominate at later times. The non-local γ-ray heating leads to significant energy deposition in the region of electron capture elements (see, Figure 13; and Penney & Hoeflich 2014).

5.2. Spectral Analysis of the JWST Observation

The goal of this section is demonstrating constraints from the JWST spectrum of SN 2022xkq, and to take full advantage of the reduced line-blending in the MIR compared to shorter wavelengths. Optical and NIR spectral series of SN 2022xkq are presented in Pearson et al. (2024). Optical and NIR fits of our model to data of other SNe Ia have been presented and discussed previously in detail (Höflich 1995; Wheeler et al. 1998; Höflich et al. 2002; Hoeflich et al. 2023; Diamond et al. 2015; Telesco et al. 2015). We focus on the MIR-spectra because interstellar reddening hardly affects the MIR fluxes; the reddening corrections are below the S/N. Studies using observations from JWST have found that the effect of reddening on the flux varies between $\sim$0.5% and 1% depending on wavelength (Gordon et al. 2023). However, the spectrophotometric accuracy of MIRI is 2%–5%. Thus, the detailed analysis of JWST MIR spectra allows the uncertainties inherent to optical wavelength range (Krisciunas et al. 2003) to be avoided. For the theoretical analysis, the focus is on line ratios between ions and the profile of features that are mostly independent from uncertainties in the distance and the reddening law. The absolute flux will be used as a consistency check between observations and models. The overall spectrum is given in Figure 14. Our spectral analysis is mostly based on Channels 1–3, because the Channel 4 spectrum requires flux calibration based upon the model flux, and the highly variable, uncertain background at the longer wavelengths makes it unsuitable for using the ionization balance or line-profiles as diagnostics.
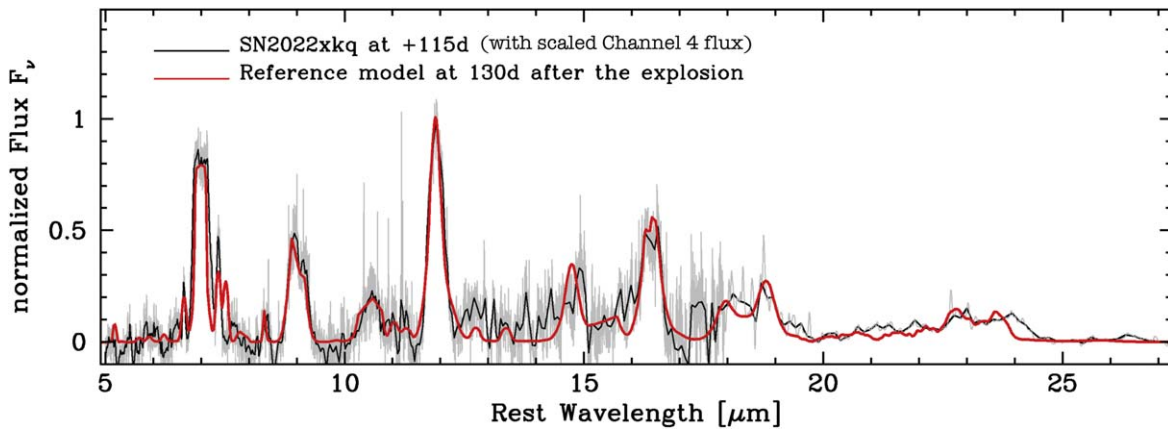
Figure 14. Comparison between the synthetic and observed MIR spectra of SN 2022xkq (black) where the flux in Channel 4 ($\lambda \geqslant 18$ μm) has been scaled to the model flux, with a wavelength-dependent scaling factor (see text).

### 5.2.1. Probing the Ionization and Abundance Structure

The comparison between the observed MIR spectrum, the spectrum of our reference model, and a low-density model is shown in Figure 15. Only the reference model matches the observations. As a reminder, the lines matching strong observed features are already discussed in Section 3 and Table 3. The full list of significant optical and IR transitions in the models is given in Tables 6 and 7, and some are marked in Figure 16. We compare F_ν because the line features depend on the lifetimes; thus, F_ν provides the proper scaling. The spectra are normalized to the [Co III]-dominated feature at 11.888 μm. From the absolute flux in our models, the normalization factor required to match the [Co III]-dominated feature at 11.888 μm corresponds to a distance modulus $\mu = 32.51$ mag. This is remarkably similar to the distance modulus derived from SN independent methods, which find $\mu = 32.46 \pm 0.15$ mag (Pearson et al. 2024).

Note that the underlying continuum flux is dominated by a quasi-continuum (Karp et al. 1977; Hoeflich et al. 1993; Hillier & Dessart 2012) produced by allowed line transitions, electron scattering, and free–free radiation in a scattering-dominated MIR photosphere expanding with a velocity of about 1500 to 2000 km s^{-1}, and particle densities of ≈ 1–2×10^7 cm^{-3}, which are close to the critical density for collisional deexcitation. Note that, based on non-LTE models, this effect was taken into account for the interpretation of many nebular spectra (e.g., Höflich et al. 2004; Diamond et al. 2015; Telesco et al. 2015; Diamond et al. 2018; DerKacy et al. 2023). The high particle density and the presence of a photosphere lead to weaker features in ^{58}Ni than expected otherwise and, potentially, blocks the emission of the most neutron-rich isotopes that form when ρ_c is high. These isotopes have been observed in SN 2016hnk (Galbany et al. 2019), and may be observed in spectra of SN 2022xkq at later epochs. Moreover, the presence of a photosphere blocks part of the redshifted emission of forbidden lines formed in the outer optically thin layers. This leads both to a blueshift versus the rest-wavelengths of transitions formed close to the photosphere (compare Figure 16 and Table 6) for SN 2022xkq. Due to the photosphere receding with time and the decreasing blocking of the redshifted emission components, the width of features by singly and doubly ionized transitions increases with time (Penney & Hoeflich 2014) as been observed in many SNe, for example, [Fe II] 1.644 μm in SN 2014J and [Co III] 11.888 μm

(Telesco et al. 2015; Diamond et al. 2018). This effect vanishes by day ≈ 200. Note that, in general, the shift of both the blended and unblended features of SN 2022xkq and the models are consistent within the spectral resolution (Figure 15). Here, the blueshifts in the almost unblended [Ni II] at 6.636 μm are -460 ± 110 km s^{-1} in the observation (Figure 4) compared to ~ -400 km s^{-1} in the model (Figure 16). Penney & Hoeflich (2014) found a shift of ≈ 2000 km s^{-1} at day 100 for normal-luminosity models with a photosphere at ≈ 5500 km s^{-1}. The velocity shift is larger because the photosphere forms farther out.

Another effect of the presence of the photosphere is a slight asymmetry in the line profile, not to be mistaken with overall asymmetries in the ejecta (Penney & Hoeflich 2014). Overall, the synthetic and observed spectra agree well (Figure 16). Most features are blended with weak transitions (Table 6). The main features in the model are at 7 μm ([Ar II], [Ni I–III]), 9 μm ([Ar III], [Ni IV]), a group at 10.6 μm ([S IV], [Co II], [Ni IV]), 11.8 μm ([Co III], with some [Co I] and [Fe II]), 14.8–16.0 μm ([Co II], [Co III]], [Fe II]), 16.3 [Co III], [Fe II], and 17.5–19 μm ([Fe II], [S III]). Additionally, some weaker features of [Ti II] can be seen at 9.19 μm (Table 6), expected for lower luminosity SNe Ia, and placing SN 2022xkq at the lower end of transitional SNe Ia.

In Channel 4, the strong features only become apparent in the spectrum of SN 2022xkq after scaling the flux by the synthetic spectrum (Figure 17). The scaling factor is wavelength-dependent and varies from a value of about 1 at 18 μm to about 50 at 26 μm. Overall, the spectra in Channel 4 are dominated by blends of singly and doubly ionized Fe and Co with peaks at ~ 18, 23, and 24 μm. In our models, the [S III] at 18.713 μm dominates the feature at 19 μm. Mixing on scales of the positron mean free path would further enhance this feature. The effect is similar to results on the photospheric S I at 1.0821 μm (Diamond et al. 2015). Even without mixing, the [S III] feature is an indication of a massive progenitor. $M_{\rm Ch}$ models produce a large amount of IMEs at the expense ejecta undergoing burning to NSE. In the models, we see a hint of the [S I] feature at 25 μm. It is not prominent because the direct and significant heating by γ-rays leads to mostly ionized S II (Figure 13). This feature is expected to grow with time as heating will transition from γ-rays to positrons by ≈ 200–300 days. At wavelengths longwards of 18 μm, the appearance of [S III] is a direct consequence of the large amount of Si and S characteristic of $M_{\rm Ch}$ scenarios. Note the possible importance of high S/N observations in the MIRI/
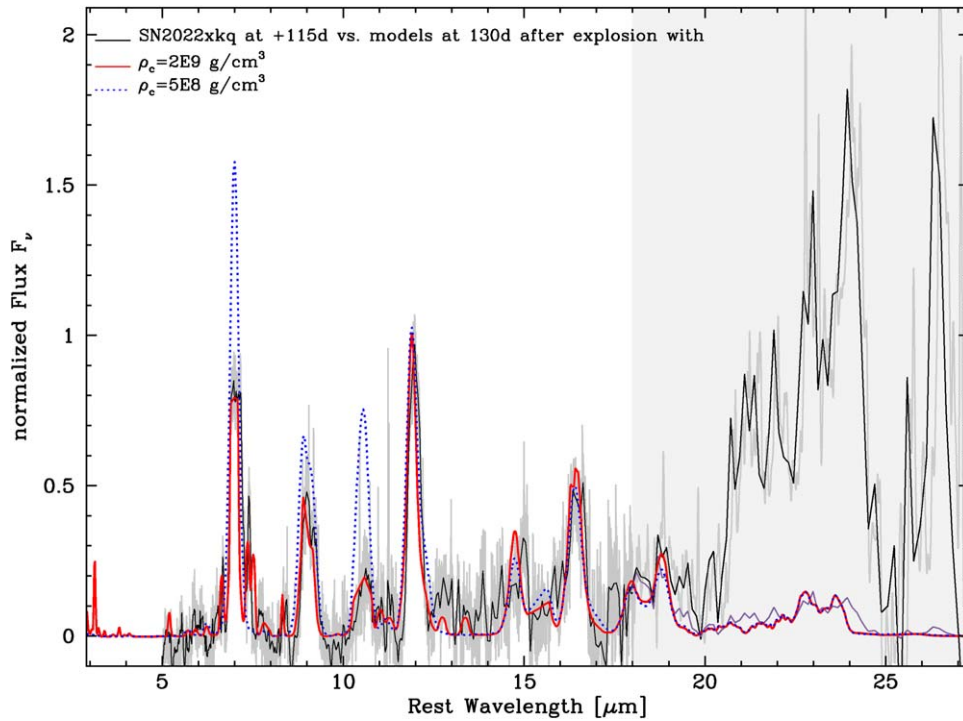
Figure 15. Comparison between the MIR spectra of SN 2022xkq in MIRI/MRS Channels 1–3 (solid black) and models with $\rho_c = 2 \times 10^9$ g cm^{-3} (solid red) and 5×10^8 g cm^{-3} (dotted blue) some 130 days after the explosion. The Channel 4 spectrum scaled to the flux level of the synthetic model spectrum using 3 μm wide bins outside of the strong features is also shown (violet). The spectra in F_ν have been normalized to the peak of the [Co III] at 11.888 μm corresponding to a distance module of 32.52 mag for our reference model. Note the strong [Ni I] feature at 3.12 μm in the models (see text). The low central density model strongly overpredicts the flux in the 7 and 9 μm [Ar] features as well as the 10.6 μm [Ni II]/[Co II] blend because the energy input is shifted to higher-density material. Higher-density models show smaller effects on the spectrum than low-density models (see text).

MRS Channel 4 to probe for ρ_c larger than 4×10^9 g cm^{-3}, because lines of [Cr V] and [Mn IV] would appear at 19.62 and 22.08 μm, respectively.

For many of the elements, multiple ionization stages are present, which lends support to the ionization structure discussed above. Within $M_{\rm Ch}$ scenarios, lower densities significantly degrade the fit by boosting the emission by features dominated by [Co II] at 10.6 μm. In our models, lower ρ_c results in more heating by ^{56}Co at lower velocity as the size of the electron capture region recedes. This shifts a significant amount of energy input into the high-density region with the lower ionization stage dominating (Figure 13), shifting the [Co III]/[Co II] ratio. With the spectra normalized to [Co III] and little effect due to Ar, the corresponding features (e.g., 7, 9 μm) appear more prominent.

Our best-fit model produces $\sim 6 \times 10^{-2}$ $M_\odot$ of ^{58}Ni. About 50% of it is located within the photosphere. Mixing of the innermost regions may expose a larger fraction of the ^{58}Ni, but as discussed below, the narrow Ni lines put strong limits on extended mixing. Note that we cannot exclude higher central density models as used in Galbany et al. (2019) because the highest-density burning layers, with the lowest electron/neutron ratio, Y_e would be hidden below the photosphere (see Figures 25–26 in Galbany et al. 2019). The [Ni I] line at about 7.5 μm is predicted by the model, but is clearly absent in the observation. To reproduce the model prediction of [Ni I], it would have to be blueshifted by ≈ 2500 km s^{-1} and blended (Figure 16). The shift of [Ni I] in the inner, high-density layers is due to recombination rates that depend on ρ^2. Higher ρ_c does not necessarily produce significantly more ^{58}Ni because the NSE shifts to more neutron-rich isotopes (see Figure 25 in

Galbany et al. 2019). If the ^{58}Ni forms a shell, it would be unstable to Rayleigh–Taylor (RT) mixing. Without detailed simulations, the impact on the line profile is hard to predict. The difference between the models and data can be due to several effects: (1) a higher ρ_c and a corresponding shift toward more neutron-rich isotopes reducing Y_e (Höflich et al. 1998; Brachwitz et al. 2000; Hristov et al. 2021); (2) some moderate, inhomogeneous mixing (Fesen et al. 2015); and (3) some passive drag by a turbulent field produced during the smoldering phase when the flame speed is low (close to the laminar speed) for ≈ 1–2 s prior to central ignition (Khokhlov 1995; Khokhlov et al. 1997b; Domínguez & Höflich 2000). See the velocity field shown in Figure 9 of Höflich & Stein (2002). These effects may be reproduced in a finely tuned model, which is beyond the scope of this work. We abstain from further tuning ρ_c due to the lack of high S/N spectra beyond 18 μm needed to verify the presence of neutron-rich isotopes (see C. Ashall et al. 2023, in preparation.).

5.2.2. Line Profiles

Figure 16 shows the model and observed spectra, with some of the stronger features identified. Ni lines appear from neutral through triply ionized ions. Peaked profiles for iron-group elements are the direct result of the energy input being dominated by γ-rays (Figure 16). The model predicts the correct line widths of [Co II] and [Co III].

The 7 and 9 μm features are both dominated by Ar and blended by [Ni II], but the 9 μm feature is heavily blended with [Ni IV]. Compared to normal-luminosity SNe Ia, the Ar layers are expanding at lower velocities. Within $M_{\rm Ch}$ explosions, this can be understood as a consequence of the dominant

Table 6
Infrared Line Identifications at Day 130 in Reference Model

S	λ (μm)	Ion	S	λ (μm)	Ion	S	λ (μm)	Ion	S	λ (μm)	Ion	S	λ (μm)	Ion
*	1.3209	[Fe II]		2.2187†	[Fe III]	*	5.6870†	[V I]	**	11.130	[Ni IV]	*	21.829	[Ar III]
	1.3210	[Fe I]		2.2425	[Fe III]	*	5.7044	[Co II]		11.167	[Co II]	*	22.297	[Fe I]
*	1.3281	[Fe II]		2.2443	[Fe II]		5.7391	[Fe II]	*	11.238†	[Ti II]		22.80†	[Co IV]
	1.3422	[Fe I]		2.3086	[Ni II]		5.8933	[Ni I]		11.307	[Ni I]	*	22.902	[Fe II]
	1.3556	[Fe I]		2.3486	[Fe III]		5.9395	[Co II]	***	11.888	[Co III]	***	22.925	[Fe III]
	1.3676	[Fe I]		2.3695	[Ni II]		5.9527	[Ni II]	**	12.001	[Ni I]		23.086	[Ni II]
*	1.3722	[Fe II]		2.4139	[Co I]	**	6.2135	[Co II]	*	12.1592†	[Ti II]	*	23.196	[Co II]
	1.3733	[Fe I]	*	2.5255	[Co I]		6.2730	[Co I]	**	12.255	[Co I]		23.389	[Fe III]
	1.3762	[Fe I]		2.6521	[Co I]		6.2738	[Co II]	*	12.2610	[Mn II]		24.04†	[Co IV]
	1.4055	[Co II]		2.7256	[Co I]		6.3683	[Ar III]	**	12.286†	[Fe II]	**	24.042	[Fe I]
*	1.4434	[Fe I]	*	2.8713	[Co I]		6.379	[Fe II]	**	12.642	[Fe II]	***	24.070	[Co III]
*	1.4972	[Co II]		2.8742	[Fe III]	***	6.6360	[Ni II]	*	12.681	[Co III]	***	24.519	[Fe II]
**	1.5339	[Fe II]		2.9048	[Fe III]		6.7213	[Fe II]	**	12.729	[Ni II]		24.847	[Co I]
***	1.5474	[Co II]	**	2.9114	[Ni II]	**	6.9196	[Ni II]	**	12.729	[Ni II]	***	25.249	[S I]
	1.5488	[Co III]	*	2.9542	[Co I]	***	6.9853	[Ar II]	*	12.811	[Ne II]	**	25.689	[Co II]
	1.5694	[Co II]		3.0060	[Co I]		7.0454	[Co I]		13.058	[Co I]	**	25.890	[O IV]
**	1.5999	[Fe II]		3.0305	[Co I]	*	7.103	[Co III]		13.820	[Co III]		25.986	[Co II]
	1.6073	[Si I]		3.0439	[Fe III]	*	7.1473	[Fe III]		13.924†	[Co IV]	***	25.988	[Fe II]
*	1.6267	[Co II]		3.0457	[Co I]		7.2019	[Co I]		14.006	[Co III]		26.100	[Co III]
*	1.6347	[Co II]	***	3.1200	[Ni I]	*	7.3492	[Ni III]		14.356	[Co I]		26.130	[Fe III]
***	1.6440	[Fe II]		3.2294	[Fe III]	**	7.5066	[Ni I]		14.391	[Co I]		26.601	[Fe II]
*	1.6459	[Si I]		3.3942	[Ni III]	*	7.7906	[Fe III]	**	14.739	[Co II]		27.530	[Co II]
**	1.6642	[Fe II]		3.4917	[Co III]		8.044	[Co I]	*	14.8140	[Ni I]		27.550	[Co I]
*	1.6773	[Fe II]	*	3.6334	[Co I]		8.211	[Fe III]	**	14.977	[Co II]		28.466	[Fe I]
*	1.7116	[Fe II]		3.7498	[Co I]	*	8.2825	[Co I]	***	15.459	[Co II]		29.675	[Mn II]
*	1.7289	[Co II]		3.8023	[Ni III]	*	8.2993	[Fe II]		16.299	[Co II]	***	33.038	[Fe III]
*	1.7366	[Co II]	**	3.9524	[Ni I]	***	8.405	[Ni IV]	***	16.391	[Co III]		33.481	[S III]
	1.7413	[Co III]	***	4.0763	[Fe II]	*	8.6107	[Fe III]	*	16.925	[Co I]		34.660	[Fe II]
*	1.7454	[Fe II]		4.0820	[Fe II]	*	8.6438	[Co II]	***	17.936	[Fe II]	*	34.713	[Fe I]
*	1.7976	[Fe II]	**	4.1150	[Fe II]	*	8.7325	[Fe II]	*	18.2410	[Ni II]	***	34.815	[Si II]
*	1.8005	[Fe II]	*	4.3071	[Co II]	*	8.9147†	[Ti II]		18.265	[Co I]	***	35.349	[Fe II]
*	1.8099	[Fe II]		4.5196	[Ni I]	**	8.945	[Ni IV]	*	18.390	[Co II]	*	35.777	[Fe II]
	1.8119	[Fe II]	**	4.6077	[Fe II]	***	8.9914	[Ar III]	***	18.713	[S III]		38.801	[Fe I]
*	1.9040	[Co II]	**	4.7881	[Ni I]	*	9.1969†	[Ti II]		18.804	[Co II]		39.272	[Co II]
**	1.9393	[Ni II]		4.8603	[Fe III]		9.279†	[Co IV]		18.985	[Co II]	***	51.301	[Fe II]
	1.9581	[Co III]	**	4.8891	[Fe II]	*	9.618	[Ni II]	*	19.0070	[Fe II]	***	51.770	[Fe III]
	2.0028	[Co III]		5.0623	[Co I]		9.8195	[Co I]	**	19.056	[Fe II]		54.311	[Fe I]
	2.0073	[Fe II]		5.1635	[Co I]	*	10.080	[Ni II]		19.138	[Ni II]	*	56.311	[S I]
	2.0418	[Ti II]	*	5.1796	[Co II]	**	10.1637†	[Ti II]		19.232	[Fe III]		60.128	[Fe II]
*	2.0466	[Fe I]	**	5.1865	[Ni II]	**	10.1890	[Fe II]		20.167	[Fe III]		…	…
	2.0492	[Ni II]		5.2112	[Co I]		10.2030	[Fe III]		20.928†	[Fe II]		…	…
	2.0979	[Co III]		5.3402	[Fe II]	*	10.5105	[Ti II]		21.17†	[Fe I]		…	…
	2.1334	[Fe II]		5.4394	[Co II]	*	10.5105	[S IV]		21.986†	[Fe II]		…	…
	2.1457	[Fe III]		5.4652†	[V I]	***	10.523	[Co II]		22.106†	[Ni I]		…	…
	2.1605	[Ti II]	*	5.6739	[Fe II]	**	10.682	[Ni II]	*	21.4810	[Fe II]		…	…

Note. The relative strengths are indicated by the number of *. For transitions without known lifetimes (marked by †), $A_{i,j}$ are assumed from the equivalent iron levels. The transitions observed in SN 2022xkq above the threshold flux level are listed in Table 3.

production of quasi statistical equilibrium in low luminosity SNe. As a consequence, in underluminous SNe, Ar (and Ca) are elements formed during the breakout to NSE and appear at lower velocities, resulting in narrower profiles. The profile is mostly flat, but narrower compared to previously observed normal-luminosity SN Ia (Figure 7). As a result, the Ni features in the blue end of the 7 μm profile are well separated from the strongest [Ni II] line at 6.636 μm although somewhat con-taminated by the weak Ni II at 6.920 μm. Note that the [Ar II]-dominated 7 μm feature has a "*dome-shaped*" rounded top produced by a narrow line-blending rather than asymmetry, with a velocity corresponding to ≈3800 km s^{-1}, consistent with the central hole in the argon distribution (Figure 12). The 7 μm feature is slightly too narrow compared to the

observation, which may indicate some RT driven mixing. In the model, the dome shape is produced by [Ni II]. While our models cannot explicitly discriminate between whether the dome shape is due to the [Ni II] blend or if the model is slightly too dim, the presence of the small [Ni I] feature suggests that it is slightly too dim.

In contrast, the 9 μm [Ar II] profile is heavily distorted/tilted by *low velocity* [Ni IV] (and some [Ti II]). The synthetic and the observed profiles are due to blending. The result is an asymmetric, peaked profile, making it unusable as an indicator for chemical asymmetry in the explosion.

The narrower [Co III] at 11.888 μm found in SN 2022xkq as compared to normal-luminosity SNe Ia is consistent with the fact that the NSE region becomes more concentrated toward the

inner region in underluminous SNe Ia; or more precisely, the QSE region grows at the expense of NSE elements (Hoeflich & Khokhlov 1996; Höflich et al. 2002; Ashall et al. 2018; Mazzali et al. 2020; see also Section 4.2.3). It is amplified by the blocking due to the photosphere that cuts off parts of the redshifted contribution to the line emission (see Section 5.2.1).

The model successfully reproduces the narrow [Ni II] and [Ni IV] lines observed providing a possible path to probing the physics of the thermonuclear runaway. Within the framework of M_{Ch} explosions, the ignition process and its location are highly debated, ranging from central ignition (Khokhlov et al. 1993; Gamezo et al. 2003) to multispot ignition in ≈ 100 spots distributed over more than 100 km (Seitenzahl et al. 2013). Detailed simulations of the simmering phase suggest a single-spot ignition close to the center at ≈ 35–50 km s^{-1} (Höflich et al. 2002; Zingale et al. 2011), but possibly out to 100 km s^{-1} (Zingale et al. 2011). For the normal-bright SN 2021aefx, Blondin et al. (2023) found that the delayed detonation model based on a strong off-center multispot ignition (Seitenzahl et al. 2013) fails to reproduce the strength of Ni lines by factors of 2 to 3, whereas delayed-detonation models starting from a single-spot ignition can reproduce the Ni lines within the model uncertainties (DerKacy et al. 2023). For SN 2022xkq, we find good agreement in the Ni lines with single-spot ignition. Because the early deflagration phase may be similar, this may indicate that single-spot ignition is common.

5.2.3. Alternative Scenarios

Detailed spectral fits of a wide variety of scenarios are beyond the scope of this paper, but constraints can be found by combining spectral indicators.

The observed [Co II]/[Co III] ratio requires high ρ_c, compared to normal-luminosity SNe Ia (Diamond et al. 2015; Telesco et al. 2015; Diamond et al. 2018) in M_{Ch} explosions, because more electron capture shifts the emission powered by radioactive decays toward lower densities. In contrast, for sub-M_{Ch} mass explosions such as helium-triggered detonations (Shen et al. 2018; Polin et al. 2019; Boos et al. 2021) or low-density mergers (García-Berro et al. 2017), lowering M_{WD} and ρ_c will decrease the average density of spectral formation, reducing the average [Co II]/[Co III] ratio. One of the effects that changes the ionization balance is the overall flatter density distribution in the initial sub-M_{Ch} WD (see Figure 18); the other is the lowering of binding energy with decreasing M_{WD}, which changes the velocity distribution of the ejecta. Sub-M_{Ch} explosions can produce an underluminous SNe Ia like SN 2022xkq for progenitors with $0.9 \leqslant M_{WD} \leqslant 1.0\ M_\odot$, but the central densities are too low for the production of electron capture elements. However, stable Ni is seen in SN 2022xkq.

In the case of a sub-M_{Ch} WD, a low Y_e may be inherited from the progenitor, due to an overabundance of ^{22}Ne produced during the stellar burning in massive stars. As suggested by Blondin et al. (2022), super-solar metallicity will shift Y_e resulting in the production of ^{58}Ni in ^{56}Ni in the QSE regions resulting in ^{58}Ni features as broad as the nebular ^{56}Co line. However, the Ni lines in SN 2022xkq are narrow (FWHM ≈ 2, 500 km s^{-1}, Figures 4, 16), while sub-M_{Ch} models show FWHM of ≈ 10, 000 km s^{-1} (see, e.g., Shen et al. 2018), excluding this path.

Alternatively, a low Y_e and, thus, some central Ni may be produced in sub-M_{Ch} progenitor systems that contain very old

WDs. Over timescales of ~ 5 billion years, gravitationally driven diffusion may allow ^{22}Ne settling in the core of a crystallized WD (Deloye & Bildsten 2002). For an initial composition of solar metallicity, the amount may or may not be sufficient to account for some [Ni II] emission observed at about 1.9 μm in some other SNe Ia (e.g., Friesen et al. 2014; Diamond et al. 2015; Hoeflich et al. 2021; Blondin et al. 2023). However, in SN 2022xkq, we see Ni in all ionization stages. The amount of stable Ni produced in old, low mass WDs is too small by a factor of 3–4 to account for the observed line strengths. The factor needs to be even larger because old stars in spiral galaxies have subsolar metallicities. Moreover, the ^{58}Ni would settle at velocities below the photosphere at 130 days after the explosion, requiring mixing.

Other alternative scenarios are dynamical mergers of two WDs where the C/O is ignited on dynamical timescales by interaction: (a) starting with grazing incidence (classical mergers), (b) violent mergers, or (c) direct collisions (Benz et al. 1990; Rosswog et al. 2009; Kushnir et al. 2013; Pakmor et al. 2013; García-Berro et al. 2017). All three would lead to asymmetric envelopes in density or abundance structures.

Unlike the 35 normal-bright SNe Ia (Cikota et al. 2019) for which polarization has been observed, the underluminous SN 1999by and SN 2005ke show a qualitatively different polarization spectrum around peak brightness, indicating an overall rotationally symmetric photosphere with an axis ratio of ≈ 0.9 based on detailed non-LTE models (Howell 2001; Patat et al. 2012). Dynamical mergers have been suggested and discussed as possible alternatives to M_{Ch} explosions of rapidly rotating WDs opening up the possibility that underluminous SNe Ia are a population distinct from normal-bright SNe Ia (Patat et al. 2012; Hoeflich et al. 2023). So far, no late-time spectropolarimetry has been obtained for underluminous SNe Ia that would produce the flip in the polarization angle in configurations found in head-on collisions of two WDs (Höflich 1995; Bulla et al. 2016).

The intermediate state in classical mergers (for almost all mass ratios between the WDs) produces a puffed up, low-density quasi-hydrostatic phase without the production of a significant amount of stable Ni (for a review, see García-Berro et al. 2017). However, violent mergers can produce a lot of ^{58}Ni and show strong MIR Ni features. In fact, the strength of the Ni features far exceeds the observations of the overluminous SN 2023pul (Kwok et al. 2023b) and the underluminous SN 2022xkq. For both SNe Ia in the MIR, the observed MIR [Ar II] lines are too strong, and the MIR Ni features are too weak compared to the model by an order of magnitude. However, it is unclear whether this is a generic property of this class of explosions.

A direct collision with parameters closer to those suggested for the underluminous SN 2007on may be more likely (Mazzali et al. 2018). This scenario, however, resulted in the ignition of both WDs, a "double line" pattern in all elements, and a significant shift in Ni (≈ 1500–3000 km s^{-1}, Dong et al. 2015; Mazzali et al. 2018; Vallely et al. 2020). Neither of these effects are compatible with SN 2022xkq unless seen "*equator-on*". In addition, we see only one component in the narrow Ni line severely limiting even small deviations from the equatorial viewing direction, unless only one of the WDs is close to M_{Ch}. We note that polarization spectra and their evolution would be very unlike the two underluminous SNe Ia mentioned above. We consider WD collisions as the explosion mechanism for
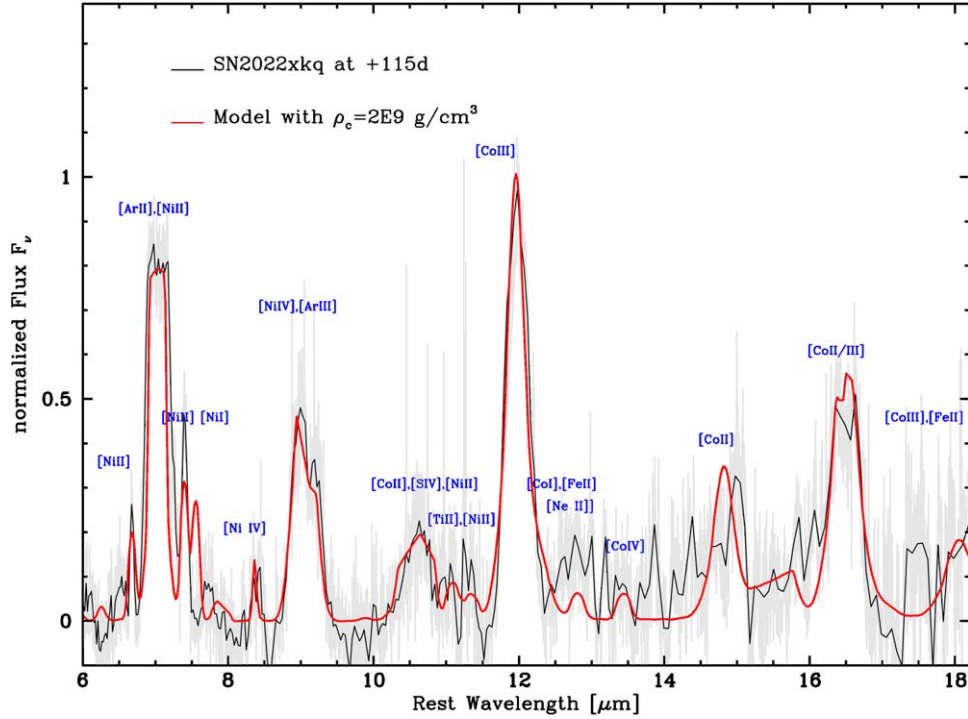
Figure 16. Same as Figure 15 with the observed spectrum for Channels 1–3 compared to the reference model, but with a tighter wavelength range. Strong features relevant for our interpretation are labeled. Note that many are blends (Table 6). Overall, the profiles of the synthetic and observed features are in good agreement. The peaks of many lines that form close to the photosphere are blueshifted due to the blocking effect of the photosphere. However, the synthetic [Ni I] line at $\approx$7.5 μm, and [Ni II] at $\approx$7.4 μm are too strong and slightly too weak, respectively compared to the observations, suggesting a slightly higher nonthermal excitation in the center of SN 2022xkq than predicted by the model, or inhomogeneous mixing.
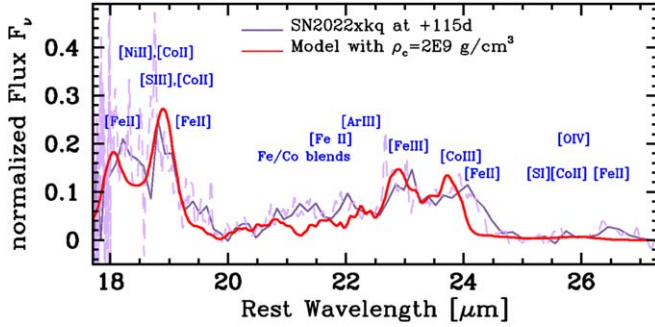
Figure 17. Same as Figure 15 with the observed, calibrated spectrum in Channel 4 with (violet) and without smoothing (light violet) compared to the reference model (red). Strong features relevant for our interpretation are labeled. Note that many are blends (Table 6). Overall, the synthetic and observed strong features are in reasonable agreement. Note the strong [S III] is indicative for a high mass WD (see text).
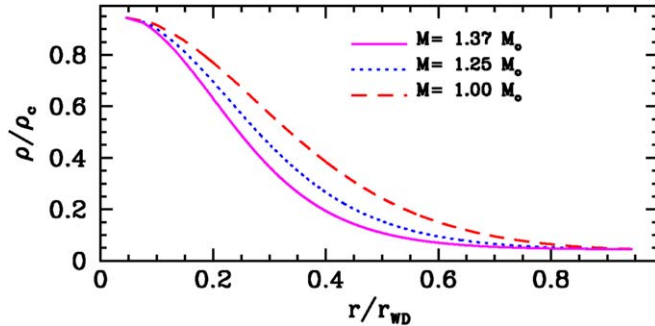
Figure 18. Normalized density as a function of radius. With increasing mass, they become more centrally concentrated (from Hoeflich 2017). Note that M(WD) $\approx$1.25 $M_\odot$ is the dividing line between M_{Ch} and sub-M_{Ch} explosions.

SN 2022xkq to be unlikely, but without detailed modeling (beyond the scope of this work), we cannot definitely rule them out.

6. Results

The main findings of our analysis are as follows:

1. The spectrum of the underluminous SN 2022xkq is distinct compared to spectra of normal-luminosity SNe Ia. The MRS/MIRI spectrum permits many detailed inferences including the first lines identified beyond 14 μm in SN Ia observations. These newly identified lines include [Co II]-dominated blends between 14 and 17 μm, and complex blends of several iron-group elements with contributions from [S III], [Ar II], [S I], and [O IV] at $\lambda > 18$ μm.

2. The identification of [Ti II] lines in the blended MIR features is consistent with SN 2022xkq being an underluminous SN Ia.

3. The stronger ratio of [Ar II]/[Ar III] in SN 2022xkq relative to the normal-luminosity spectra at similar epochs suggests a shift in the ionization balance toward singly ionized species over doubly ionized ones.

4. In observations at these phases, line formation is a complex mixture of allowed lines, forbidden transitions, a pseudo-continuum, and other radiative transfer effects. The combination of fits and data driven measurements to the [Ni II] 6.636 μm, [Ni III] 7.349 μm, and [Co III] 11.888 μm lines reveal the following: a) that the peaks of the IGEs are blueshifted by $\sim$200–400 km s^{-1} relative to the rest wavelength of the dominant line; and b) that these features

are narrow in width when compared to the same lines in normal-luminosity SNe Ia. Fitting of the line profiles with simple analytic functions (e.g., Gaussians) must be approached with caution as they do not capture the complex line formation physics, even in some isolated lines with little blending.

5. A tentative correlation is seen between the FWHM of the [Co III] 11.888 μm resonance line and the light-curve shape parameter $\Delta m_{15}(B)$. This relationship is consistent with the ^{56}Ni being produced in NSE burning occurring closer to the center in underluminous objects. Future MIR observations should continue to add to this plot to see if it follows the luminosity-width relation observed in the optical.

6. The light-curve properties (Table 5) of the model are consistent with the early time data of SN 2022xkq (Pearson et al. 2024), as well as other underluminous SNe Ia such as SN 2007on and SN 2011iv (Gall et al. 2018). While SN 2022xkq is at the lower luminosity end of the transitional SNe Ia distribution, it is significantly (1.5 mag) brighter than SN 1991bg-like objects (Section 5).

7. The spectral characteristics can be understood within the framework of high-density burning in a delayed-detonation model in which somewhat more mass is consumed in the deflagration prior to the onset of the DDT, seen equator-on (Figure 15). In particular, the shift from a predominately doubly ionized spectrum to a mix of ionization I-III is consistent with the low luminosity. The shift in the ionization balance toward lower stages is obvious (Figure 13 and Section 5.2.1). Moreover, the strongest features in the models are also the strongest features observed, and all weak features in the observations have their equivalent in the model (compare Table 3 with Table 6).

8. Electron capture in the central region has a significant impact on the spectra: With increasing ρ_c, the higher average density shifts the ionization balance from [Co III] to [Co II]. As a result, the [Co II] lines are stronger (Figure 15). Furthermore, the large number of Ni features indicates electron capture (Table 6).

9. The sensitivity of intermediate mass versus iron-group elements and the important role of high resolution in the MIR accessible with JWST have been demonstrated as a key to constrain the underlying physics and to test models (Figure 15).

10. At ~130 days after explosion, the spectra form during the onset of the nebular phase. In our models, the optical to MIR photosphere is formed by a quasi-continuum at $\approx$2000 km s^{-1} hiding the innermost layers. This photospheric blocking is consistent with the shift of the peak of the emission features relative to the rest wavelength by a few hundred kilometers per second (Figures 7 and 16). As discussed in Section 5.1, only some of the electron capture elements in the models are above the photosphere, and potentially, electron capture elements such as Cr, and Mn are hidden. Within the framework of $M_{\rm Ch}$ mass explosions, the central density of the WD $\rho_c = 2 \times 10^9$ g cm^{-3} and the ^{58}Ni mass may be regarded as a lower limit.

11. SN 2022xkq is likely to have been observed close to "*equator-on*", and/or the point of the DDT is within the low-velocity distribution of ^{56}Ni (Sections 5.2.1 and 5.2.2). Line polarization should be largest when seen from near to the equator, but vanishes when seen from other inclinations showing the importance of spectropolarimetry during the photospheric phase.

12. The line profiles of [Ar II] and [Co III] show a narrow flat top and are rounded, respectively. This is expected from underluminous models for the explosion of a massive WD with large pre-expansion during the deflagration phase prior to the DDT, resulting in overall an increased production of IMEs (Si/S/Ca/Ar) compared to that produced in normal-luminosity SNe Ia (Figure 7).

13. The [Ar III] profile at 9 μm is strongly tilted because it is contaminated by Ti and Ni blends. In underluminous SNe Ia, it cannot be used to infer asymmetry in the density distribution (Section 5.2.2).

14. The line profile of [Ar II] at 7 μm is better suited to deciphering the location of the DDT and the viewing angle of underluminous SN Ia. This is because line-blending is reduced due to the lower overall velocities. The size of the *Ar hole* is slightly smaller in our models than inferred from the observations, but suggests that SN 2022xkq is seen from the equator. The domed-shaped profile is a result of line-blending and not asymmetry (Section 5.2.2).

15. The [Co III] feature at 11.888 μm shows a rounded, broad profile characteristic for a central ^{56}Ni-free region. This is also supported by and consistent with the numerous narrow ^{58}Ni lines (Section 5.2.1).

16. The strong [S III] at $\approx$19 μm is indicative of a massive WD; as in underluminous SNe Ia, the IME production is increased compared to normal-luminosity SNe Ia (see Figures 14 and 17).

17. In underluminous SNe Ia, the ionization balance is shifted toward lower states (Figure 13), and in the central region, neutral IGEs become significant. This is also seen as a the lower half width of both electron capture lines and lines from neutral Fe, Co, Ni when compared to normal-luminosity SNe Ia.

18. The lines of stable ^{58}Ni are clearly identified and are consistent between models and observations. At ~130 days past the explosion, the densities of the central region remained high, $>10^7$ g cm^{-3} up to $\approx$2000 km s^{-1} resulting in Ni emission less pronounced than expected in the nebular phase (Section 5). The narrow ^{58}Ni lines suggest a central ignition mixing of electron capture elements produced by preexisting turbulent fields rather than by RT-instabilities as would be expected from multispot, off-center ignition (Section 5.2.2).

19. A central DDT white C/O-rich material mixed-down can all but be excluded because the ^{58}Ni lines are narrow. For the first time, this may constrain the mechanisms possible for the DDT (Sections 5 and 5.2.2).

20. The synthetic fluxes in MIR spectra (Section 5.2) are consistent with the observations of SN 2022xkq. The MIR has the advantage of insensitivity to reddening.

7. Discussion

Compared to previous low-resolution observations, the additional insight afforded by MIRI/MRS is readily apparent, especially as it relates to the increased wavelength coverage of MRS relative to LRS and the higher resolution. In SN 2022xkq,

the additional wavelength coverage reveals multiple [Co]-dominated features in the 14–17 μm range, as well as complex blends of select transitions from [O], [S], and [Ar] along with many blended features comprised of [Fe], [Ni], and [Co] lines beyond ∼20 μm.

The decrease in velocity errors from $\gtrsim$2000 to ∼100 km s^{-1} allows us to accurately measure small-scale velocity line shifts (see Figures 4, 5 and 6), to assess whether they originate from asymmetries (such as those originating from off-center DDTs), line formation effects, or temporal evolution from sources such as positron transport (at later epochs). This increased resolution also affords us the ability to better determine the shape of line profiles throughout the spectrum. In particular, the width and shape of the [Ar II] and [Ar III] lines from weak blends permit the estimation of the viewing angle of the SN if observed at the appropriate epochs. Furthermore, these Ar lines probe the transition between the NSE and QSE regions during burning and provide clear discriminators between different explosion models. Finally, the increase in resolution compared to LRS data allows for previously blended lines to be resolved, such as the [Ni II] 6.636 μm and [Ni III] 7.349 μm lines. This provides tighter constraints on the physical conditions present in the ejecta.

The apparent correlation between the FWHM of the [Co III] 11.888 μm line and the light-curve shape parameter offer tantalizing hope for the existence of an MIR spectroscopic luminosity-width relation that may be similar to the luminosity-width relation (Phillips 1993). As more data are added to this plot, the relationship may provide an independent method to calculate the luminosity of an SN Ia with a single nebular-phase spectrum. Over the coming years, as the sample of MIR spectra from JWST grows, this relationship can be tested.

Unlike the traditional luminosity-width relation, determining whether an SN Ia meets the criteria for inclusion on the MIR luminosity-width plot (Figure 11) is less straightforward. In order for such a measurement to accurately probe this relation, the SN must be in the nebular phase with little to no contamination from an underlying photosphere, ^{56}Co decay must be the dominant source of energy deposition in the ejecta, and the strength of the weak blends of [Fe III] and [Ni I] should be low. In the context of M_{Ch} explosions, this phase will occur earlier in less luminous objects and later in more luminous ones. The specific timing of this window will vary from object to object due to differences in the physical conditions of the ejecta, but the spectroscopic observations targeting the ∼100–300 days window should meet these conditions in most SNe Ia.

SN 2022xkq is one of the most extensively observed underluminous SN Ia ever, with an early time data set starting hours after explosion and spanning from the ultraviolet to the near-infrared (Pearson et al. 2024). Yet, this extensive data set does not conclusively point toward a specific origin for SN 2022xkq. With the addition of the MIR observations presented here, a clearer picture emerges. The early time presence of carbon points toward unburnt material in the outer layers, which naturally arise in the M_{Ch} model presented here. The lack of bimodality in the [Co III] 11.888 μm line and the MIR electron capture lines (e.g., ^{58}Ni) located interior to the ^{56}Ni region disfavor a collision; the lack of late-time O lines seen in the MIR disfavors a merger; and the presence of strong electron capture lines favors high-density burning in the ejecta. This highlights the importance of multiepoch, multiwavelength observations of SNe Ia to determine the specific origins of individual objects.

Finally, we mention some limitations that will be overcome in the future. JWST is still in the early stages of operation. The data reduction and calibration will improve, in particular at longer wavelengths. Moreover, additional later-time spectra will be needed to see the innermost region. Due to both of these effects, we could only obtain a lower limit upon electron capture elements such as Cr, Mn that have strong transitions beyond 18 μm. Detecting these lines would further refine the central density and the degree of mixing as these lines will only be present in models with $\rho_c \gtrsim 4 \times 10^9$ g cm^{-3}. Estimates of the cross sections for many transitions of iron group elements will be obtained by calibration of bright SNe Ia, as the cross sections are not available for many transitions, for example those of [Ti II].

8. Conclusion

We present an MIRI MIR spectrum of the underluminous SN Ia, SN 2022xkq, obtained at +114.2 days past maximum light. These are the first JWST observations of an underluminous SN Ia and the first lines identified beyond 14 μm in SNe Ia observations. The data show evidence of isolated narrow lines of stable Ni emission, and strong emission from Ar and Co. In contrast to normal-luminosity SNe Ia, SN 2022xkq shows lower ionization states; in particular, it contains more [Ar II] relative to [Ar III]. Furthermore, the velocity extent of the resonance [Co III] feature is narrower compared to more luminous SNe Ia observed at roughly the same phase. This indicates the ^{56}Ni is closer to the core of the explosion. We also find a potential correlation between the FWHM of the [Co III] resonance feature and the light-curve shape parameter $\Delta m_{15}(B)$. Observing more SNe Ia at this phase will allow us to understand if this follows the luminosity-width relation for SNe Ia.

By comparing the data to newly synthesized non-LTE models, we determine that the presence of narrow forbidden Ni lines is strong evidence for the explosion of a massive WD. The presence of multiple [Ti II] lines is consistent with SN 2022xkq's location at the low luminosity end of this class. We show that the MIR spectra and the absolute flux can be well understood within an off-center delayed-detonation scenario seen equator-on with a peak luminosity ∼1.2 mag below normal SNe Ia. The spectra also hint that the SN had a central thermodynamic runaway and only a moderate off-set of the DDT. The strong IME elements and low luminosity suggest, at least in some SNe Ia, the lower luminosity is not correlated with a lower total WD mass.

This work demonstrates the power of using JWST data in combination with detailed simulations; especially, the wavelength coverage beyond 14 μm provided by MIRI/MRS. Looking ahead, harnessing this capability through forthcoming observations promises to usher us into a new era of SNe Ia physics.

Appendix A
Optical Lines at Day 130 after the Explosion

Line identifications, as determined from the best-fitting model in the optical are listed in Table 7.

Table 7
Optical Line Identifications at Day 130 in Reference Model

S	λ (μm)	Ion	S	λ (μm)	Ion	S	λ (μm)	Ion	S	λ (μm)	Ion	S	λ (μm)	Ion
	0.3689	[Co II]		0.4641	[Fe II]		0.5562	[Co II]		0.8030	[Co II]		0.9697	[Co I]
	0.4104	[Co II]	*	0.4659	[Fe II]	*	0.5890	[Co III]	**	0.8123	[Co II]		0.9705	[Fe III]
	0.4154	[Co II]		0.4703	[Fe III]		0.5908	[Co III]		0.8123	[Co II]		0.9946	[Co II]
	0.4178	[Fe II]		0.4729	[Fe II]		0.6072	[Co I]		0.8303	[Ni II]	***	0.9946	[Co II]
*	0.4245	[Fe II]		0.4735	[Fe III]		0.6129	[Co III]	***	0.8336	[Co II]		1.0191	[Co II]
	0.4246	[Fe II]		0.4749	[Co II]		0.6197	[Co III]	**	0.8466	[Co II]		1.0248	[Co II]
	0.4278	[Fe II]		0.4756	[Fe III]		0.6578	[Co III]		0.8469	[Co II]		1.0283	[Co II]
*	0.4289	[Fe II]		0.4771	[Fe III]		0.6586	[Co I]		0.8502	[Ni III]	*	1.0283	[Co II]
	0.4307	[Fe II]		0.4804	[Co II]		0.6669	[Ni II]		0.8546	[Co I]		1.0611	[Fe III]
	0.4321	[Fe II]		0.4882	[Fe III]		0.6855	[Co III]	*	0.8574	[Co II]		1.0718	[Ni II]
	0.4327	[Ni II]		0.4891	[Fe II]		0.6934	[Co II]		0.8583	[Co II]		1.0718	[Ni II]
	0.4348	[Fe II]		0.4932	[Fe III]		0.7138	[Ar III]		0.8597	[Co I]	**	1.0824	[S I]
	0.4354	[Fe II]	*	0.5013	[Fe III]		0.7155	[Co III]	**	0.8619	[Fe II]		1.0885	[Fe III]
	0.4360	[Fe II]		0.5086	[Fe III]	**	0.7157	[Fe II]	*	0.8894	[Fe II]	*	1.0976	[Co II]
	0.4361	[Fe II]		0.5113	[Fe II]	*	0.7174	[Fe II]		0.9036	[Fe II]		1.0994	[Si I]
	0.4374	[Fe II]	*	0.5160	[Fe II]		0.7249	[Co I]		0.9054	[Fe II]	*	1.1283	[Co II]
	0.4415	[Fe II]		0.5222	[Fe II]	**	0.7293	[Ca II]		0.9071	[S III]	*	1.1309	[S I]
	0.4418	[Fe II]	*	0.5263	[Fe II]	**	0.7326	[Ca II]		0.9229	[Fe II]		1.1616	[Ni II]
	0.4453	[Fe II]		0.5270	[Co II]	**	0.7380	[Ni II]		0.9270	[Fe II]		1.2489	[Fe II]
	0.4459	[Fe II]	*	0.5272	[Fe III]		0.7390	[Fe II]	**	0.9339	[Co II]		1.2525	[Fe II]
	0.4476	[Fe II]		0.5298	[Fe II]	*	0.7414	[Ni II]	***	0.9345	[Co II]	***	1.2570	[Fe II]
	0.4490	[Fe II]		0.5335	[Fe II]	*	0.7455	[Fe II]		0.9447	[Fe III]	*	1.2707	[Fe II]
	0.4494	[Fe II]		0.5378	[Fe II]		0.7541	[Co II]		0.9474	[Fe II]	*	1.2791	[Fe II]
	0.4501	[Co III]		0.5414	[Fe III]		0.7640	[Fe II]		0.9533	[S III]	*	1.2946	[Fe II]
	0.4608	[Fe III]		0.5472	[Co II]		0.7689	[Fe II]		0.9642	[Co II]		1.2981	[Fe II]
	0.4624	[Co II]		0.5548	[Co II]	*	0.7892	[Ni III]		0.9642	[Co II]		…	…

Note. The relative strengths are indicated by the number of * as in Table 6.

ORCID iDs

J. M. DerKacy ⓘ https://orcid.org/0000-0002-7566-6080
C. Ashall ⓘ https://orcid.org/0000-0002-5221-7557
P. Hoeflich ⓘ https://orcid.org/0000-0002-4338-6586
E. Baron ⓘ https://orcid.org/0000-0001-5393-1608
M. Shahbandeh ⓘ https://orcid.org/0000-0002-9301-5302
B. J. Shappee ⓘ https://orcid.org/0000-0003-4631-1149
J. Andrews ⓘ https://orcid.org/0000-0003-0123-0062
D. Baade ⓘ https://orcid.org/0000-0003-1637-9679
K. A. Bostroem ⓘ https://orcid.org/0000-0002-4924-444X
P. J. Brown ⓘ https://orcid.org/0000-0001-6272-5507
C. R. Burns ⓘ https://orcid.org/0000-0003-4625-6629
A. Burrow ⓘ https://orcid.org/0000-0002-5380-0816
A. Cikota ⓘ https://orcid.org/0000-0001-7101-9831
T. de Jaeger ⓘ https://orcid.org/0000-0001-6069-1139
A. Do ⓘ https://orcid.org/0000-0003-3429-7845
Y. Dong ⓘ https://orcid.org/0000-0002-7937-6371
I. Dominguez ⓘ https://orcid.org/0000-0002-3827-4731
O. Fox ⓘ https://orcid.org/0000-0003-2238-1572
L. Galbany ⓘ https://orcid.org/0000-0002-1296-6887
E. T. Hoang ⓘ https://orcid.org/0000-0003-2744-4755
E. Y. Hsiao ⓘ https://orcid.org/0000-0003-1039-2928
D. Janzen ⓘ https://orcid.org/0000-0003-0549-3281
J. E. Jencson ⓘ https://orcid.org/0000-0001-5754-4007
K. Krisciunas ⓘ https://orcid.org/0000-0002-6650-694X
S. Kumar ⓘ https://orcid.org/0000-0001-8367-7591
J. Lu ⓘ https://orcid.org/0000-0002-3900-1452
M. Lundquist ⓘ https://orcid.org/0000-0001-9589-3793
T. B. Mera Evans ⓘ https://orcid.org/0000-0001-5888-2542
J. R. Maund ⓘ https://orcid.org/0000-0003-0733-7215
P. Mazzali ⓘ https://orcid.org/0000-0001-6876-8284
K. Medler ⓘ https://orcid.org/0000-0001-7186-105X
N. E. Meza Retamal ⓘ https://orcid.org/0000-0002-7015-3446
N. Morrell ⓘ https://orcid.org/0000-0003-2535-3091
F. Patat ⓘ https://orcid.org/0000-0002-0537-3573
J. Pearson ⓘ https://orcid.org/0000-0002-0744-0047
M. M. Phillips ⓘ https://orcid.org/0000-0003-2734-0796
M. Shrestha ⓘ https://orcid.org/0000-0002-4022-1874
S. Stangl ⓘ https://orcid.org/0000-0001-5570-6666
C. P. Stevens ⓘ https://orcid.org/0000-0003-0763-6004
M. D. Stritzinger ⓘ https://orcid.org/0000-0002-5571-1833
N. B. Suntzeff ⓘ https://orcid.org/0000-0002-8102-181X
C. M. Telesco ⓘ https://orcid.org/0000-0002-0036-9292
M. A. Tucker ⓘ https://orcid.org/0000-0002-2471-8442
S. Valenti ⓘ https://orcid.org/0000-0001-8818-0795
L. Wang ⓘ https://orcid.org/0000-0001-7092-9374
Y. Yang ⓘ https://orcid.org/0000-0002-6535-8500

References

Argyriou, I., Glasse, A., Law, D. R., et al. 2023, A&A, 675, A111
Arnett, W. D. 1982, ApJ, 253, 785
Arnett, W. D., Branch, D., & Wheeler, J. C. 1985, Natur, 314, 337
Ashall, C., Lu, J., Hsiao, E. Y., et al. 2021, ApJ, 922, 205
Ashall, C., Mazzali, P., Sasdelli, M., & Prentice, S. J. 2016a, MNRAS, 460, 3529
Ashall, C., Mazzali, P. A., Pian, E., & James, P. A. 2016b, MNRAS, 463, 1891
Ashall, C., Mazzali, P. A., Stritzinger, M. D., et al. 2018, MNRAS, 477, 153
Astropy Collaboration, Price-Whelan, A. M., Lim, P. L., et al. 2022, ApJ, 935, 167
Astropy Collaboration, Price-Whelan, A. M., Sipőcz, B. M., et al. 2018, AJ, 156, 123
Astropy Collaboration, Robitaille, T. P., Tollerud, E. J., et al. 2013, A&A, 558, A33

Bell, J. B., Day, M. S., Rendleman, C. A., Woosley, S. E., & Zingale, M. 2004, ApJ, 606, 1029
Benetti, S., Cappellaro, E., Mazzali, P. A., et al. 2005, ApJ, 623, 1011
Benz, W., Bowers, R. L., Cameron, A. G. W., & Press, W. H. 1990, ApJ, 348, 647
Blondin, S., Bravo, E., Timmes, F. X., Dessart, L., & Hillier, D. J. 2022, A&A, 660, A96
Blondin, S., Dessart, L., Hillier, D. J., Ramsbottom, C. A., & Storey, P. J. 2023, A&A, 678, A170
Bloom, J. S., Kasen, D., Shen, K. J., et al. 2012, ApJL, 744, L17
Boos, S. J., Townsley, D. M., Shen, K. J., Caldwell, S., & Miles, B. J. 2021, ApJ, 919, 126
Brachwitz, F., Dean, D. J., Hix, W. R., et al. 2000, ApJ, 536, 934
Branch, D., Dang, L. C., Hall, N., et al. 2006, PASP, 118, 560
Branch, D., Romanishin, W., & Baron, E. 1996, ApJ, 465, 73
Bravo, E., García-Senz, D., Cabezón, R. M., & Domínguez, I. 2009, ApJ, 695, 1257
Brooker, E., Plewa, T., & Fenn, D. 2021, MNRAS, 501, L23
Bulla, M., Sim, S. A., Pakmor, R., et al. 2016, MNRAS, 455, 1060
Burns, C. R., Stritzinger, M., Phillips, M. M., et al. 2011, AJ, 141, 19
Burns, C. R., Stritzinger, M., Phillips, M. M., et al. 2014, ApJ, 789, 32
Burrow, A., Baron, E., Ashall, C., et al. 2020, ApJ, 901, 154
Bushouse, H., Eisenhamer, J., Dencheva, N., et al. 2023, JWST Calibration Pipeline, v1.12.1, Zenodo, doi:10.5281/zenodo.8380331
Charignon, C., & Chièze, J. P. 2013, A&A, 550, A105
Chen, P., Bruch, R., Zimmerman, E., et al. 2022a, Transient Name Server Classification Report, 2022-2975, TNS
Chen, P., Schulze, S., Sollerman, J., & Maguire, K. 2022b, Transient Name Server Classification Report, 2022-3026, TNS
Cikota, A., Patat, F., Wang, L., et al. 2019, MNRAS, 490, 578
de Vaucouleurs, G., de Vaucouleurs, A., Corwin, H. G. J., et al. 1991, Third Reference Catalogue of Bright Galaxies (New York: Springer)
Deloye, C. J., & Bildsten, L. 2002, ApJ, 580, 1077
DerKacy, J. M., Ashall, C., Hoeflich, P., et al. 2023, ApJL, 945, L2
Dessart, L., Hillier, D. J., Blondin, S., & Khokhlov, A. 2014, MNRAS, 439, 3114
Dhawan, S., Flörs, A., Leibundgut, B., et al. 2018, A&A, 619, A102
Diamond, T. R., Hoeflich, P., & Gerardy, C. L. 2015, ApJ, 806, 107
Diamond, T. R., Hoeflich, P., Hsiao, E. Y., et al. 2018, ApJ, 861, 119
Domínguez, I., & Höflich, P. 2000, ApJ, 528, 854
Dong, S., Katz, B., Kushnir, D., & Prieto, J. L. 2015, MNRAS, 454, L61
Döring, W. 1943, AnP, 435, 421
Fesen, R. A., Höflich, P. A., & Hamilton, A. J. S. 2015, ApJ, 804, 140
Filippenko, A. V., Richmond, M. W., Branch, D., et al. 1992a, AJ, 104, 1543
Filippenko, A. V., Richmond, M. W., Matheson, T., et al. 1992b, ApJL, 384, L15
Foley, R. J., Challis, P. J., Chornock, R., et al. 2013, ApJ, 767, 57
Friesen, R. K., Di Francesco, J., Bourke, T. L., et al. 2014, ApJ, 797, 27
Galbany, L., Ashall, C., Höflich, P., et al. 2019, A&A, 630, A76
Gall, C., Stritzinger, M. D., Ashall, C., et al. 2018, A&A, 611, A58
Gamezo, V. N., Khokhlov, A. M., Oran, E. S., Chtchelkanova, A. Y., & Rosenberg, R. O. 2003, Sci, 299, 77
García-Berro, E., Badenes, C., Aznar-Siguán, G., & Lorén-Aguilar, P. 2017, MNRAS, 468, 4815
Garnavich, P. M., Bonanos, A. Z., Krisciunas, K., et al. 2004, ApJ, 613, 1120
Gerardy, C. L., Meikle, W. P. S., Kotak, R., et al. 2007, ApJ, 661, 995
Gordon, K. 2023, karllark/dust_extinction: OneRelationForAllWaves, v1.2, Zenodo, doi:10.5281/zenodo.7799360
Gordon, K. D., Clayton, G. C., Decleir, M., et al. 2023, ApJ, 950, 86
Graham, M. L., Kennedy, T. D., Kumar, S., et al. 2022, MNRAS, 511, 3682
Hamuy, M., Phillips, M. M., Suntzeff, N. B., et al. 1996, AJ, 112, 2391
Harris, C. R., Millman, K. J., van der Walt, S. J., et al. 2020, Natur, 585, 357
Hicken, M., Garnavich, P. M., Prieto, J. L., et al. 2007, ApJL, 669, L17
Hillier, D. J., & Dessart, L. 2012, MNRAS, 424, 252
Hoeflich, P. 2017, in Handbook of Supernovae, ed. A. W. Alsabti & P. Murdin (Berlin: Springer), 1151
Hoeflich, P., Ashall, C., Bose, S., et al. 2021, ApJ, 922, 186
Hoeflich, P., Hsiao, E. Y., Ashall, C., et al. 2017, ApJ, 846, 58
Hoeflich, P., & Khokhlov, A. 1996, ApJ, 457, 500
Hoeflich, P., Mueller, E., & Khokhlov, A. 1993, A&A, 268, 570
Hoeflich, P., Yang, Y., Baade, D., et al. 2023, MNRAS, 520, 560
Höflich, P. 1995, ApJ, 443, 89
Höflich, P. 2006, NuPhA, 777, 579
Höflich, P. 2009, in AIP Conf. Proc. 1171, Recent Directions in Astrophysical Quantitative Spectroscopy and Radiation Hydrodynamics, ed. I. Hubeny et al. (San Francisco, CA: ASP), 161

Höflich, P., Gerardy, C., Linder, E., et al. 2003, in Stellar Candles for the Extragalactic Distance Scale, ed. D. Alloin & W. Gieren (Berlin: Springer), 203
Höflich, P., Gerardy, C. L., Fesen, R. A., & Sakai, S. 2002, ApJ, 568, 791
Höflich, P., Gerardy, C. L., Nomoto, K., et al. 2004, ApJ, 617, 1258
Hoflich, P., Khokhlov, A., & Wheeler, C. 1995, in ASP Conf. Ser. 73, From Gas to Stars to Dust, ed. M. R. Haas, J. A. Davidson, & E. F. Erickson (San Francisco, CA: ASP), 441
Höflich, P., & Stein, J. 2002, ApJ, 568, 779
Höflich, P., & Wheeler, J. C., & Thielemann, F. K. 1998, ApJ, 495, 617
Hoogendam, W. B., Ashall, C., Galbany, L., et al. 2022, ApJ, 928, 103
Hosseinzadeh, G., Jha, S. W., Bostroem, K. A., et al. 2022, Transient Name Server Classification Report, 2022-2987, TNS
Howell, D. A. 2001, ApJL, 554, L193
Howell, D. A., Sullivan, M., Nugent, P. E., et al. 2006, Natur, 443, 308
Hoyle, F., & Fowler, W. A. 1960, ApJ, 132, 565
Hristov, B., Collins, D. C., Hoeflich, P., Weatherford, C. A., & Diamond, T. R. 2018, ApJ, 858, 13
Hristov, B., Hoeflich, P., & Collins, D. C. 2021, ApJ, 923, 210
Hsiao, E. Y., Hoeflich, P., Ashall, C., et al. 2020, ApJ, 900, 140
Hunter, J. D. 2007, CSE, 9, 90
Iben, I. J., & Tutukov, A. V. 1984, ApJS, 54, 335
Janzen, D., Valenti, S., Bostroem, K. A., et al. 2022, Transient Name Server Discovery Report, 2022-2969, TNS
Jha, S. W. 2017, in Handbook of Supernovae, ed. A. W. Alsabti & P. Murdin (Berlin: Springer), 375
Karp, A. H., Lasher, G., Chan, K. L., & Salpeter, E. E. 1977, ApJ, 214, 161
Kendrew, S., Scheithauer, S., Bouchet, P., et al. 2015, PASP, 127, 623
Khokhlov, A., Mueller, E., & Hoeflich, P. 1993, A&A, 270, 223
Khokhlov, A. M. 1991, A&A, 245, 114
Khokhlov, A. M. 1995, ApJ, 449, 695
Khokhlov, A. M., Oran, E. S., & Wheeler, J. C. 1997a, ApJ, 478, 678
Khokhlov, A. M., Oran, E. S., & Wheeler, J. C. 1997b, in Proc. NATO Advanced Study Institute, ed. P. Ruiz-Lapuente, R. Canal, & J. Isern (Dordrecht: Kluwer), 475
Koribalski, B. S., Staveley-Smith, L., Kilborn, V. A., et al. 2004, AJ, 128, 16
Krisciunas, K., Suntzeff, N. B., Candia, P., et al. 2003, AJ, 125, 166
Krisciunas, K., Suntzeff, N. B., Espinoza, J., et al. 2017, RNAAS, 1, 36
Kuchner, M. J., Kirshner, R. P., Pinto, P. A., & Leibundgut, B. 1994, ApJL, 426, L89
Kushnir, D., Katz, B., Dong, S., Livne, E., & Fernández, R. 2013, ApJL, 778, L37
Kwok, L. A., Jha, S. W., Temim, T., et al. 2023a, ApJL, 944, L3
Kwok, L. A., Siebert, M. R., Johansson, J., et al. 2023b, arXiv:2308.12450
Leibundgut, B., Kirshner, R. P., Phillips, M. M., et al. 1993, AJ, 105, 301
Leloudas, G., Stritzinger, M. D., Sollerman, J., et al. 2009, A&A, 505, 265
Li, W., Filippenko, A. V., Chornock, R., et al. 2003, PASP, 115, 453
Li, Z., Zhang, T., Wang, X., et al. 2022, ApJ, 927, 142
Livne, E. 1999, ApJL, 527, L97
Livne, E., & Arnett, D. 1995, ApJ, 452, 62
Lu, J., Ashall, C., Hsiao, E. Y., et al. 2021, ApJ, 920, 107
Maguire, K., Sim, S. A., Shingles, L., et al. 2018, MNRAS, 477, 3567
Marion, G. H., Sand, D. J., Hsiao, E. Y., et al. 2015, ApJ, 798, 39
Mazzali, P. A., Ashall, C., Pian, E., et al. 2018, MNRAS, 476, 2905
Mazzali, P. A., Bikmaev, I., Sunyaev, R., et al. 2020, MNRAS, 494, 2809
Mazzali, P. A., Cappellaro, E., Danziger, I. J., Turatto, M., & Benetti, S. 1998, ApJL, 499, L49
Mazzali, P. A., Chugai, N., Turatto, M., et al. 1997, MNRAS, 284, 151
Mazzali, P. A., Röpke, F. K., Benetti, S., & Hillebrandt, W. 2007, Sci, 315, 825
Meikle, W. P. S., Spyromilio, J., Allen, D. A., Varani, G. F., & Cumming, R. J. 1993, MNRAS, 261, 535
Mould, J. R., Huchra, J. P., Freedman, W. L., et al. 2000, ApJ, 529, 786
Niemeyer, J. C., & Woosley, S. E. 1997, ApJ, 475, 740
Nomoto, K., Sugimoto, D., & Neo, S. 1976, Ap&SS, 39, L37
Nomoto, K., Thielemann, F. K., & Yokoi, K. 1984, ApJ, 286, 644
Nugent, A. E., Polin, A. E., & Nugent, P. E. 2023, arXiv:2304.10601

Nugent, P., Phillips, M., Baron, E., Branch, D., & Hauschildt, P. 1995, ApJL, 455, L147
Oran, E. S. 2011, in AIP Conf. Ser. 1376, Recent Progresses in Fluid Dynamics Research, ed. J. Li & S. Fu (Melville, NY: AIP), 38
Pakmor, R., Kromer, M., Taubenberger, S., et al. 2012, ApJL, 747, L10
Pakmor, R., Kromer, M., Taubenberger, S., & Springel, V. 2013, ApJL, 770, L8
Patat, F., Höflich, P., Baade, D., et al. 2012, A&A, 545, A7
Pearson, J., Sand, D. J., Lundqvist, P., et al. 2024, ApJ, in press (arXiv:2309.10054)
Pejcha, O., Antognini, J. M., Shappee, B. J., & Thompson, T. A. 2013, MNRAS, 435, 943
Penney, R., & Hoeflich, P. 2014, ApJ, 795, 84
Perlmutter, S., Aldering, G., Goldhaber, G., et al. 1999, ApJ, 517, 565
Phillips, M. M. 1993, ApJL, 413, L105
Phillips, M. M., Ashall, C., Burns, C. R., et al. 2022, ApJ, 938, 47
Phillips, M. M., Phillips, A. C., Heathcote, S. R., et al. 1987, PASP, 99, 592
Phillips, M. M., Wells, L. A., Suntzeff, N. B., et al. 1992, AJ, 103, 1632
Pinto, P. A., & Eastman, R. G. 2000a, ApJ, 530, 744
Pinto, P. A., & Eastman, R. G. 2000b, ApJ, 530, 757
Polin, A., Nugent, P., & Kasen, D. 2019, ApJ, 873, 84
Poludnenko, A. Y., Chambers, J., Ahmed, K., Gamezo, V. N., & Taylor, B. D. 2019, Sci, 366, aau7365
Ratay, D. L. 2004, PhD thesis, Univ. Florida
Rieke, G. H., Wright, G. S., Böker, T., et al. 2015, PASP, 127, 584
Riess, A. G., Filippenko, A. V., Challis, P., et al. 1998, AJ, 116, 1009
Rigby, J., Perrin, M., McElwain, M., et al. 2023, PASP, 135, 048001
Rosswog, S., Kasen, D., Guillochon, J., & Ramirez-Ruiz, E. 2009, ApJL, 705, L128
Ryder, S. D., Alsaberi, R. Z. E., Anderson, G., et al. 2022, ATel, 15687, 1
Scalzo, R. A., Aldering, G., Antilogus, P., et al. 2010, ApJ, 713, 1073
Schlafly, E. F., & Finkbeiner, D. P. 2011, ApJ, 737, 103
Seitenzahl, I. R., Ciaraldi-Schoolmann, F., Röpke, F. K., et al. 2013, MNRAS, 429, 1156
Seitenzahl, I. R., & Townsley, D. M. 2017, in Handbook of Supernovae, ed. A. W. Alsabti & P. Murdin (Berlin: Springer), 1955
Shappee, B. J., & Thompson, T. A. 2013, ApJ, 766, 64
Shen, K. J., Kasen, D., Miles, B. J., & Townsley, D. M. 2018, ApJ, 854, 52
Siebert, M. R., Kwok, L. A., Johansson, J., et al. 2024, ApJ, in press (arXiv:2308.12449)
Soker, N., Kashi, A., García-Berro, E., Torres, S., & Camacho, J. 2013, MNRAS, 431, 1541
Stritzinger, M., Mazzali, P. A., Sollerman, J., & Benetti, S. 2006, A&A, 460, 793
Sullivan, M., Conley, A., Howell, D. A., et al. 2010, MNRAS, 406, 782
Takáts, K., Pignata, G., Pumo, M. L., et al. 2015, MNRAS, 450, 3137
Tartaglia, L., Sand, D. J., Valenti, S., et al. 2018, ApJ, 853, 62
Telesco, C. M., Höflich, P., Li, D., et al. 2015, ApJ, 798, 93
Thompson, T. A. 2011, ApJ, 741, 82
Vallely, P. J., Tucker, M. A., Shappee, B. J., et al. 2020, MNRAS, 492, 3553
van Hoof, P. A. M. 2018, Galax, 6, 63
Virtanen, P., Gommers, R., Oliphant, T. E., et al. 2020, NatMe, 17, 261
von Neumann, J. 1942, Progress Report 549, OSRD
Wang, X., Filippenko, A. V., Ganeshalingam, M., et al. 2009, ApJL, 699, L139
Webbink, R. F. 1984, ApJ, 277, 355
Wells, M., Pel, J. W., Glasse, A., et al. 2015, PASP, 127, 646
Wheeler, J. C., Höflich, P., Harkness, R. P., & Spyromilio, J. 1998, ApJ, 496, 908
Whelan, J., & Iben, I. J. 1973, ApJ, 186, 1007
Wilk, K. D., Hillier, D. J., & Dessart, L. 2018, MNRAS, 474, 3187
Wilk, K. D., Hillier, D. J., & Dessart, L. 2020, MNRAS, 494, 2221
Woosley, S. E., & Weaver, T. A. 1994, ApJ, 423, 371
Yang, J., Wang, L., Suntzeff, N., et al. 2022, ApJ, 938, 83
Yoon, S. C., Langer, N., & Scheithauer, S. 2004, A&A, 425, 217
Zel'dovich, Y. B. 1940, ZhETF, 10, 524
Zingale, M., Nonaka, A., Almgren, A. S., et al. 2011, ApJ, 740, 8